

# Predicting Large Ocean Wave Events Characterized by Bimodal Energy Spectra in the Presence of a Low-Level Southerly Wind Feature

ASHLEY ELLENSON

*School of Civil and Construction Engineering, Oregon State University, Corvallis, Oregon*

H. TUBA ÖZKAN-HALLER

*College of Earth, Ocean, and Atmospheric Sciences, Oregon State University, Corvallis, Oregon*

(Manuscript received 17 March 2017, in final form 16 January 2018)

## ABSTRACT

Three large wave events are simulated with WaveWatch III using different wind inputs and physics packages. The modeled output, including spectral shape and bulk parameter time series, are compared with National Data Buoy Center buoy observations offshore of Newport, Oregon. The atmospheric conditions that generate these large waves include a strong southerly wind along with a distant cyclone. The energetic contributions of these simultaneously occurring atmospheric features result in a wave field characterized by bimodal energy spectra for two events and unimodal energy spectra for the third event. The analysis of model output evaluates bulk parameter time series of significant wave height, mean period, and mean wave direction derived from partitioned energy spectra. A consistent underestimation in wave energy approaching from the southwestern direction is found for the output associated with all model configurations. This wave energy is generated by the southerly wind. An overestimation in swell energy approaching from the northwest is also found for all model configurations. The model configuration that most accurately reproduces the southerly wave energy results in the best performance for the overall bulk parameters.

## 1. Introduction

Large wave heights pose dangers to those engaging in maritime activities, physical risk to coastal infrastructure, and hazards to residents and recreational beach users. A system that can accurately predict the characteristics of large sea states (including information about bulk parameters such as wave height, period, and direction, or more detailed quantities such as directional wave spectra) is important for quantifying the risk associated with large wave events. Such a system can provide timely information that can guide emergency response procedures or inform marine users about when marine conditions are safe enough to interface with the ocean.

Wave predictions can be made on global or regional scales (Fan et al. 2012; Monbaliu et al. 2000). The range of scales allows for the implementation of wave predictions in different contexts. Global predictions can be used to assess potential resources for wave energy

harvesting or the exploration of Earth system interactions such as air–sea energy fluxes (Arinaga and Cheung 2012; Rascle et al. 2008). Regional wave models can be coupled with tidal and surge models to simulate coastal flooding or can be configured in a way to optimize local predictions (Wolf 2009; Alves et al. 2014). Generally, these wave models are implemented after being assessed over a period of many years in order to determine model performance during a variety of conditions and seasonal cycles. Case studies of wave events often focus on times of high wave hazard in order to determine the model configurations that perform best during such conditions (Padilla-Hernández et al. 2007; Tolman et al. 2005). While much research has been performed on the simulation of wave fields during typhoons or tropical storms (e.g., Moon et al. 2003; Hu and Chen 2011; Esquivel-Trava et al. 2015), more research of model performance during large wave conditions in extratropical regions is warranted.

Although wave predictions have become increasingly more accurate over the last few decades, studies of long-term wave hindcasts suggest that wave model predictions

---

*Corresponding author:* Ashley Ellenson, ellensoa@oregonstate.edu

underestimate large wave heights associated with the peaks of wave height time series (Bidlot et al. 2002). This is especially problematic because accurate forecasts are most critical during large wave conditions that pose the greatest risk to coastal residents and infrastructure. Given the intuitive knowledge of model underprediction during storms, National Weather Service forecasters treat the forecast model output as guidance and routinely alter the predicted wave heights during large wave conditions before issuing their official forecasts (Chawla et al. 2013b). Although this intuitive understanding is useful, informing efforts to improve the forecast modeling system necessitates a more systematic understanding of the model error. Such a systematic understanding can be realized by comparing a model hindcast that encompasses various storm conditions to observations and detailing the nature of the model error and its relationship to the environmental conditions. More specifically, disagreements between the model and observations provide opportunities to learn more about the environmental context surrounding model deficiencies. This knowledge can result in more accurate quantification and communication of forecast uncertainty and can inform future research aimed at improving critical model parameterizations of physical processes.

Spectral wave propagation models are the standard tool for producing wave forecasts, and their output is sensitive to input variables, such as the wind forcing, or parameterizations of physical processes. Therefore, errors in the prediction of large wave conditions can broadly be linked to errors in the input fields, inadequacies in the spatial or temporal resolution of the input fields and model grids, or inaccuracies in the parameterizations of physical processes. For example, it has been shown that the quality of the model input, specifically atmospheric forcing, will directly affect wave model skill (Cavaleri 2009). Predicting highly energetic and fast-moving atmospheric features that lead to large wave conditions can be especially difficult (Bidlot et al. 2002), and this can contribute to larger wave prediction errors during large wave conditions. Simulations that utilize different combinations of wind input and parameterizations of physical processes (model physics) clearly suggest that a more accurate wind input will yield a more accurate wave model output (Behrens and Günther 2009; Cavaleri 2009; Rogers et al. 2007). The accuracy of the wind input can be related to the quality of the atmospheric model that was used but can also be a function of model resolution, especially in the case of atmospheric features that are constrained in space, such as tropical cyclones, which can be hard to capture with a coarsely resolved wind product (Timmermans et al. 2017). The challenge in capturing the effects of these atmospheric features on the marine environment can be further

complicated at land–sea transitions. These transitions demand higher resolution in models as well as a careful interpolation of wind products. (Chawla et al. 2013a,b). Finally, wave models employ various parameterizations to account for processes related to sources and sinks of wave energy (such as wind forcing or whitecapping dissipation). Also critical are parameterizations that govern the changes in an established swell field as it travels through a local storm feature. Identifying key parameterizations that are responsible for wave model inaccuracies can lead to targeted work to remedy issues and improve predictions (Ardhuin et al. 2007).

Large wave height events that are associated with cyclones often involve bimodal conditions, wherein both sea (short period or high frequency) and swell (long period or low frequency) conditions are present. The safety hazards associated with sea and swell components differ, and it is therefore important to differentiate between the two (Chawla et al. 2013b). In wave model simulations that resolve both components, model output often results in underestimations of sea state energy at shorter periods and overestimations of swell energy at longer periods (Chawla et al. 2013b; Bidlot et al. 2002). These two errors might combine to result in a prediction of the overall bulk significant wave height that is close in value to the observed wave height, even though the model fails to accurately reproduce the nuances of the wave field (Rogers et al. 2007). Therefore, validating the model by only considering bulk parameters, such as significant wave height, may not be adequate; instead, comparisons of wave energy spectra are more appropriate to represent model skill. Spectral partitioning methods that separate the distinct energies of wind sea and swell can convey a more realistic understanding of the wave climate, especially when multiple wave energy components are often present (Kumar et al. 2012; Innocentini et al. 2014; Rapizo et al. 2015). When spectral partitioning methods are used in conjunction with physical wave theory, wave energy can be traced to the atmospheric events from which they originated (Kumar et al. 2012; Kpogonuwoklo et al. 2014; Portilla 2012).

The U.S. Pacific Northwest is an environment subject to large wave events at approximately the rate of one 10-m wave height event per year. The strongest storms produce wave heights of 14–15 m (Ruggiero et al. 2010). Studies have shown that the average annual wave height has been increasing throughout the past quarter century, and the largest wave heights are increasing at a more rapid rate than that of the average wave height (Ruggiero et al. 2010; Menéndez et al. 2008; Allan and Komar 2000; Seymour 2011). These large wave events are often forced by complicated atmospheric features, resulting in events characterized by bi- or multimodal

wave energy spectra. This makes the U.S. Pacific Northwest an ideal location for evaluating the performance of wave models in predicting such ocean states.

In this study, we address the challenges of modeling a high-energy wave field at the land–sea boundary forced by fast-moving atmospheric features of high wind speed ( $25 \text{ m s}^{-1}$ ). We utilize a hindcast of wave conditions that was performed for the coasts of Oregon and southwest Washington using a spectral wave propagation model (García-Medina et al. 2014). The hindcast, originally carried out for applications within the renewable energy sector, provides information on the spatial and temporal variability of the wave field along the coastline. Herein, reductions in overall and partitioned bulk parameter error are made in the hindcast output of events associated with large waves. These events are characterized by wave heights exceeding 6 m for over 5 h. We begin with a description of the typical atmospheric conditions, specific to the northeast Pacific Ocean, leading to a large wave event in section 2. Section 3 then describes the wave model components wind input and physics packages. Permutations of these components are implemented in four different model configurations to simulate three historical large wave events, which are described in section 4. Our analysis includes comparing the modeled output with observations to correlate specific atmospheric forcing features to model performance in section 5. This includes comparisons of the spectral output between each model configuration and observations to reveal how nuances of the wave field are reproduced. In section 6, the importance of the temporal and spatial resolution of the model components is explored by varying the resolution of these components in three additional simulations of a large wave event.

## 2. Atmospheric forcing of large wave events in the Pacific Northwest

The waves associated with large wave events can consist of long-period swell energy to short-period wind sea energy. Waves arriving at the Pacific Northwest (PNW) coastline are often generated by midlatitude cyclones. While cyclones exist throughout the Pacific Ocean, the strongest cyclones originate east of Japan and south of Alaska. After cyclogenesis, they travel several thousands of miles east and decay as they travel north. They often pass over the PNW coastline, and ultimate dissipation usually happens north of  $50^\circ$  (see Fig. 1; Graham and Diaz 2001; Gyakum et al. 1989; Komar and Allan 2000). This sequence can last several days, and pressures can drop 20–30 mb (1 mb = 1 hPa; Graham and Diaz 2001). The wave energy associated with the life cycle of a cyclone can take on several forms.

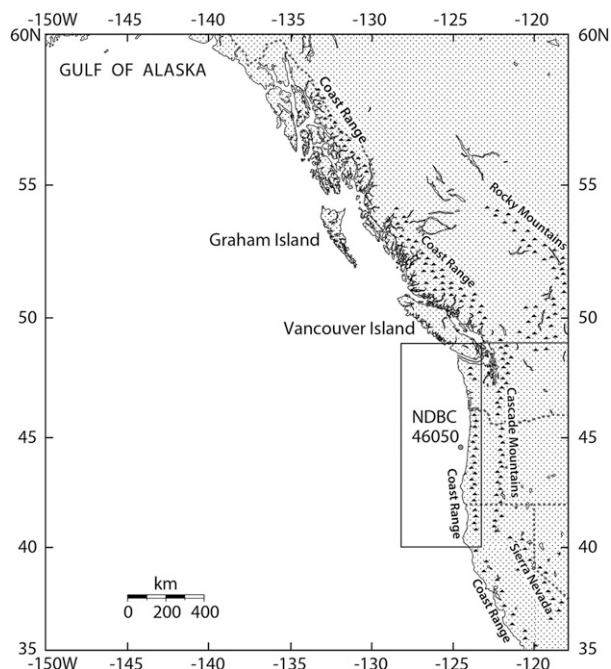


FIG. 1. The region encompassing the atmospheric features discussed in this study. The local area of interest is marked by a bounding box.

The wave energy generated as the cyclone first develops will arrive at the PNW coastline as a long-period swell. As the cyclone moves closer to the region, the wave energy will be characterized by periods that are shorter than the original incoming swell energy. The shortest wave periods (approximately 4–7 s) are generated locally, and the intermediate wave periods (approximately 8–13 s) are generated when the cyclone is at a further distance from land.

In addition to cyclones, atmospheric fronts can also generate local and far-field wave energy along the Pacific Northwest coastline. A strong southerly wind might precede the front and take the form of a low-level, shore-parallel coastal wind jet associated with the orographically induced blocking of a cold front as it travels eastward over land. Atmospheric conditions that result in the formation of this wind jet include a stable atmosphere and a cold or occluded front approaching the shoreline at an angle. If the shoreline is characterized by a steep mountain range, such as the Coast Range along the Pacific Northwest shoreline (see Fig. 1), low-level blocking of this obliquely oriented cold front may occur. Consequently, a wind maximum oriented in the north–south direction may form. This wind maximum appears as a narrow, strong, southerly wind called a coastal boundary jet, which is tightly bound to the shore. It can extend from the California–Oregon border to Vancouver Island and reach speeds

TABLE 1. Model configurations.

Model name	Physics package	Product	Wind	
			Time resolution (h)	Spatial resolution (°)
ST2-GFS	ST2	GFS	3	0.5
ST2-CFSR	ST2	CFSR	1	0.312
ST4-GFS	ST4	GFS	3	0.5
ST4-CFSR	ST4	CFSR	1	0.312

greater than  $25 \text{ m s}^{-1}$  (Doyle 1997). The results of an atmospheric modeling study found that the feature decays longitudinally, or cross shore, 5 times more quickly than latitudinally, or alongshore (Doyle 1997). This coastal jet is a specific case of a strong southerly wind preceding a cold or occluded front. Generally, a southerly wind might precede a cold or occluded front as it approaches the shoreline, even if it does not take the form of a coastal jet. The repercussion of this southerly wind in wave energy is a strong signal from the south, which can be associated with very short to intermediate (approximately 4–10 s) periods depending on the duration of the southerly wind and the fetch it encompasses. The atmospheric forcing of the events analyzed in this study feature a southerly wind primarily or in conjunction with a midlatitude cyclone, described further in section 4.

### 3. Methods

#### a. The wave model

A spectral model was implemented to assess the wave climatology for the coastlines of southeast Washington and Oregon by producing a 7-yr hindcast with WaveWatch III. The results of this hindcast are detailed in García-Medina et al. (2014). WaveWatch III (WWIII) is a spectral wave model that uses the spectral action balance equation to simulate wave energy propagation along a grid. The application of WWIII to the PNW coastline in García-Medina et al. (2014) involves three nested grids of increasing resolution. The first grid spans the entire Pacific Ocean at a 30 arc-minute resolution, the second the eastern North Pacific at a 7.5 arc-minute resolution, and the third the continental shelf ( $40.3^{\circ}$ – $49.5^{\circ}\text{N}$ ,  $233^{\circ}$ – $236.25^{\circ}\text{W}$ ) at a 90-s resolution. The first two outer grids utilize bathymetry from the National Geophysical Data Center's ETOPO1 dataset, and the innermost bathymetry is a blend of the ETOPO1 and NOAA's Gridded Tsunami Bathymetry (Amante and Eakins 2009; Carignan et al. 2009a,b,c,d; Grothe et al. 2010, 2011). The resolution for direction is  $10^{\circ}$ . The resolution for frequency begins at 0.003 Hz for the lowest frequency of 0.03 Hz and increases to 0.11 Hz for the highest frequencies (1.23 Hz is the highest frequency considered).

The simulation implements Tolman and Chalikov's (1996) ST2 physics package (hereafter referred to as ST2). It is forced every 3 h by Global Forecasting System (GFS) 10-m winds and air–sea temperature differences. This model configuration will hereafter be referred to as the original model and labeled ST2-GFS to indicate the applicable combination of physics package and wind input. Generally, the wind input is the first component to be considered to improve the wave model results, since the quality of the wave model output is directly related to the quality of the wind input. Herein, we consider the Climate Forecast System Reanalysis (CFSR) wind product produced by National Centers for Environmental Prediction (NCEP). The second component to be considered to improve the wave model results is the physics package implemented. We therefore also consider the Ardhuin et al. (2010) ST4 physics package in two model configurations (hereafter referred to as ST4). Recent literature suggests that this package better represents wind–wave and wave–wave energy transfer, thus producing more accurate wave model results (Ardhuin et al. 2010). In sum, four model configurations are considered in this study that implement permutations of the different wind input and physics packages (see Table 1).

#### 1) WIND INPUT

The two wind input datasets to be compared are NCEP's GFS and CFSR products. The GFS wind dataset has a 3-h time resolution,  $0.5^{\circ} \times 0.5^{\circ}$  spatial resolution, and is used in the original model configuration (NCEP/NWS 2007). This wind product comprises four separate models (atmospheric, oceanic, land–soil, and sea ice models) that are coupled to provide 16-day operational forecasts. In comparison, the CFSR dataset (Saha et al. 2010a) is a reanalyzed product and, therefore, benefits from the availability of observations to increase model skill. Further, it is resolved more finely in time and space, at an hourly time resolution and  $0.312^{\circ} \times 0.312^{\circ}$  spatial resolution. The same four systems (atmospheric, oceanic, land–soil, and sea ice) are coupled. The GFS model is the atmospheric model implemented in the CFSR. Improvements in the CFSR wind accuracy are largely due to data assimilation and coupling techniques (Saha et al. 2010b; Stopa and



Cheung 2014). Studies have found that the CFSR tends to overestimate moderate wind speeds and underestimate wind speeds in the 99th percentile and higher ( $\geq 15 \text{ m s}^{-1}$ ) in the northeast Pacific (Stopa and Cheung 2014).

## 2) PHYSICS PACKAGES

WaveWatch III implements the spectral balance equation where the evolution of wave energy density  $F$  is calculated as a sum of the source terms  $S_i$ :

$$\frac{dF}{dt} = \sum_i S_i. \quad (1)$$

Different physics packages implement different source terms.

The source terms considered in the ST2 physics package consist of a wind-wave interaction term, a nonlinear term that spreads energy between frequencies, and a dissipation term ( $S_{\text{wind}}$ ,  $S_{\text{nl}}$ , and  $S_{\text{ds}}$ , respectively). The wind-wave interaction term is based on Chalikov and Belevich (1993). This term allows for negative values for waves traveling at large angles with the wind and results in less energy input for fully grown seas. The nonlinear term is based on the Hasselmann and Hasselmann (1985) discrete interaction approximation (DIA). This term is known to overestimate the energy exchange at higher frequencies. To account for this overestimation, this physics package reduces the strength of this term. The dissipation term is the least studied term within this physics package and is implemented as a tuning term, which closes the spectral action balance (Tolman and Chalikov 1996). This term dissipates swell and sea-state energy differently by using two distinct formulations for energy associated with low- and high-frequency regions and also by imposing a diagnostic tail on the highest frequencies. The dissipation of lower frequencies is designed by considering turbulent viscosity in the oceanic boundary layer (Ardhuin et al. 2010). The dissipation term for the higher frequencies is diagnostic and designed to guarantee that the total sum of the source terms is balanced. At the highest frequencies, a spectral roll off to the negative fifth power (frequency  $f^{-5}$ ) is imposed (Tolman and Chalikov 1996). Note that the ST2 physics package was employed by Chawla et al. (2013a) to assemble a 30-yr wave hindcast dataset that is available for use in design applications; hence, understanding the impact of the use of this package on wave predictions should be of interest.

The second physics package used in this study, ST4, implements a different set of source terms. These include atmospheric, nonlinear, oceanic, and bottom source terms ( $S_{\text{atm}}$ ,  $S_{\text{nl}}$ ,  $S_{\text{oc}}$ , and  $S_{\text{bt}}$ , respectively). While the ST2 physics

package allows for negative wind input values in  $S_{\text{wind}}$  to incorporate the momentum flux from waves to wind, the ST4 physics package explicitly separates the momentum flux into and out of the wave field by implementing  $S_{\text{in}}$  and  $S_{\text{out}}$  components within the  $S_{\text{atm}}$  term. The  $S_{\text{out}}$  term is related to the atmospheric/oceanic boundary layer over swells and takes on different formulations with respect to the level of turbulence within the boundary layer. The wind input term  $S_{\text{in}}$  is adapted from Janssen (1991) and the subsequent modifications made by Bidlot et al. (2007). In this implementation, the wind input is reduced for high frequencies and high winds to avoid unrealistic wind stress values. This is compensated for by a tuning parameter  $\beta_{\text{max}}$ . The parameter values used in this study are provided in the wave model documentation (Tolman 2009). Specifically, this study uses TEST 451 parameter values, where  $\beta_{\text{max}}$  is set to 1.52. In the ST2 source term, dissipation occurs for lower and high frequencies separately and is meant to act as a closure term to keep the source terms in a quasi equilibrium. In the ST4 formulation, the oceanic source term  $S_{\text{oc}}$  comprises three parts: dissipation due to wave spectrum saturation, cumulative breaking, and turbulence. The cumulative breaking term represents the dissipation of smaller waves as a result of big breakers. Similar to ST2 physics, the final source term  $S_{\text{nl}}$  also implements the DIA of Hasselmann and Hasselmann (1985), albeit with a slightly smaller coefficient  $C_{\text{nl}}$  (Ardhuin et al. 2010).

Validation of the ST4 physics package by Ardhuin et al. (2010) found a general overestimation of low-frequency energy and a directional spectrum that was generally broader than that which was observed (see Fig. 2 in Ardhuin et al. 2010). The ST2 physics package tends to underestimate energy input into the spectrum by the wind for growing seas, which results in an overall underestimation of wave energy (Ardhuin et al. 2010; Kazeminezhad and Siadatmousavi 2017; Ardhuin et al. 2007).

## b. Analysis

In this study, three different large wave events are simulated with the four model configurations (ST2-GFS, ST2-CFSR, ST4-GFS, and ST4-CFSR; see Table 1). The model performance is analyzed by comparing the output with observations in section 5. The first portion of this analysis consists of bulk parameter time series comparisons. The bulk parameters significant wave height  $H_s$  and mean period  $T_m$  are compared with the bulk parameters observed at the buoy during the large wave events. Bulk parameters  $H_s$  and  $T_m$  are defined as combinations of moments derived from the energy spectrum, as in the following equations:

$$H_s = 4\sqrt{m_0} \quad \text{and} \quad (2)$$

TABLE 2. Events summary.

Event	Start date	Max $H_s$ (m)	Avg MWD (°)	Avg $T_m$ (s)	Avg wind speed ( $\text{m s}^{-1}$ )	Avg wind direction (°)	Atmospheric description
1	16 Nov 2009	9.4	221	8.4	15	198	Rapid increase in wave height; strong coastal southerly winds with three cyclones: one at Graham Island and two that occur simultaneously within 700 km NW of NDBC buoy 46050
2	19 Nov 2009	7.0	220	8.1	16	184	Consistent wave height; southerly wind disappears and reappears; winds are of smaller latitudinal extent and lesser intensity; there are two cyclones: one at Graham Island and one 400 km NW of NDBC buoy 46050
3	30 Nov 2010	7.6	210	7.2	11	181	Rapid increase in wave height; southerly wind translates south along the coast; there is one cyclone in the Gulf of Alaska

$$T_m = \frac{m_0}{m_1}, \quad (3)$$

where the  $n$ th moment  $m_n$  is defined as

$$m_n = \int_{\theta} \int_f f^n F(f, \theta) df d\theta \quad \text{for } n = 0, 1, 2, \dots \quad (4)$$

In this formulation,  $f$  is frequency and  $\theta$  is direction. To quantify the accuracy of the modeled time series of these bulk parameters, error metrics root-mean-square error (RMSE), scatter index (SI), and bias are calculated for the wave model output time series associated with the four model configurations. See [section 5](#) for this analysis.

While bulk parameters are often used to characterize wave conditions, bulk parameters might not accurately convey the details of the wave conditions, such as the contribution of each wave train to the overall significant wave height. This is because the derivation of bulk parameters requires the integration of energy spectra [see Eqs. (2)–(4)], and the details of the shape of the energy spectra are lost in this process. Therefore, to thoroughly compare the modeled output and the observations, this analysis considers the evolution of the energy spectra throughout the large wave event. This includes delineating the energy spectra into quadrants to separate each wave train and subsequently comparing the model output and observations associated with each quadrant. To quantify this comparison, time series of  $H_s$  and  $T_m$  of each quadrant and the associated error metrics are calculated. See [section 5](#) for more details about and the execution of this analysis.

#### 4. Case studies

Inspection of the hindcast by [García-Medina et al. \(2014\)](#) shows that the original model performs poorly in terms of absolute error for events where wave heights

exceeded 6 m (see the [appendix](#)). Specifically, when the hindcast output was divided into bins of significant wave height smaller than 4 m and larger than 6 m, the RMSE was increased from 0.42 to 1.34 m, and the bias was switched from an overestimation of 0.14 m to an underestimation of 0.67 m [error metrics RMSE and bias are defined as in [García-Medina et al. \(2014\)](#)]. We searched for large wave events, which were defined as  $H_s \geq 6$  m for at least 5 h, from the time series of three years of model output (2009–11). We identified approximately 12 such events and inspected these to find when the model performed particularly poorly. We found that 9 out of the 12 events featured a strong southerly wind as described in [section 2](#) either before or during the peak wave height of the event time series. Three of these storms were selected to serve as case studies for hindcast improvement and are summarized in [Table 2](#). Time series of significant wave height  $H_s$ , mean period  $T_m$ , mean wave direction (MWD), wind direction, and wind speed are presented in [Fig. 2](#).

These three events are described further as follows. First, the atmospheric conditions preceding and during the event are described. Then, the observations of  $H_s$ ,  $T_m$ , and MWD at NDBC buoy 46050 are discussed. The bulk parameter MWD is defined in [Kuik et al. \(1988\)](#). It is obtained from the first four Fourier coefficients of the directional distribution. MWD is defined in a nautical convention, where  $0^\circ$  indicates waves incident from the north,  $90^\circ$  from the east,  $180^\circ$  from the south, and  $270^\circ$  from the west. The description of the events will focus on the atmospheric features of the northeast Pacific and their locations relative to NDBC buoy 46050 ([Fig. 1](#)). This buoy is located roughly in the middle of the PNW coastline, 23 mi west of Newport, Oregon, in 137-m water depth.

##### a. Event 1

The first selected event begins at 1200 UTC 16 November 2009, when a low pressure center at

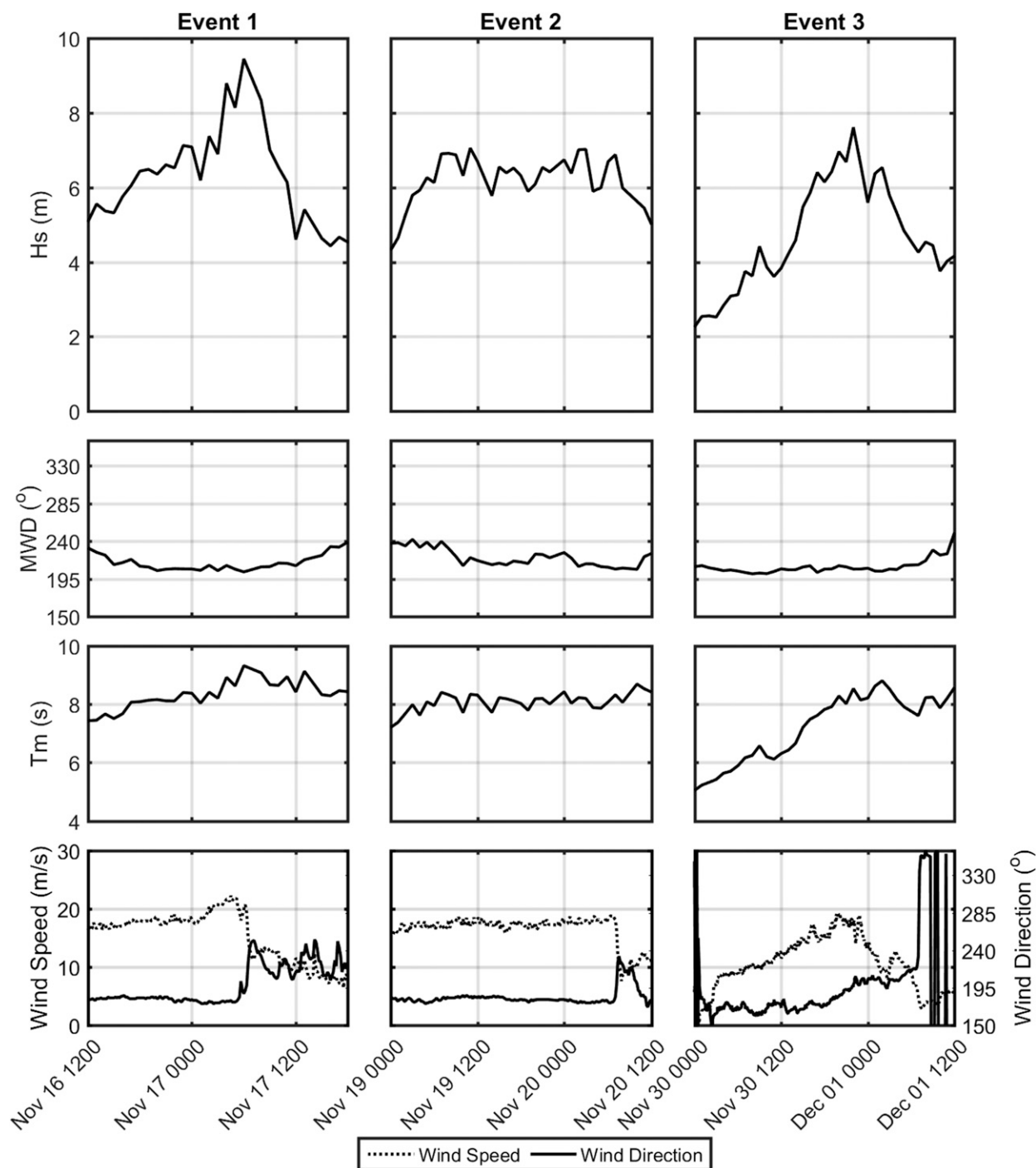


FIG. 2. The  $H_s$ , MWD,  $T_m$ , wind speed, and wind direction as observed by NDBC buoy 46050.

980 mb is located on Graham Island, off the coast of British Columbia, and a strong southerly wind extends from the California–Oregon border to the Washington–Canada border (see Fig. 3 for synoptic-scale pressure and wind maps from the CFSR). The low remains at approximately 980 mb and on Graham

Island until 2000 UTC 16 November, at which point the low pressure system dissipates. The southerly wind slowly decreases in extent during this time, with its final and shortest extent spanning from the California–Oregon border to NDBC buoy 46050. A few hours later, at 0000 UTC 17 November, another

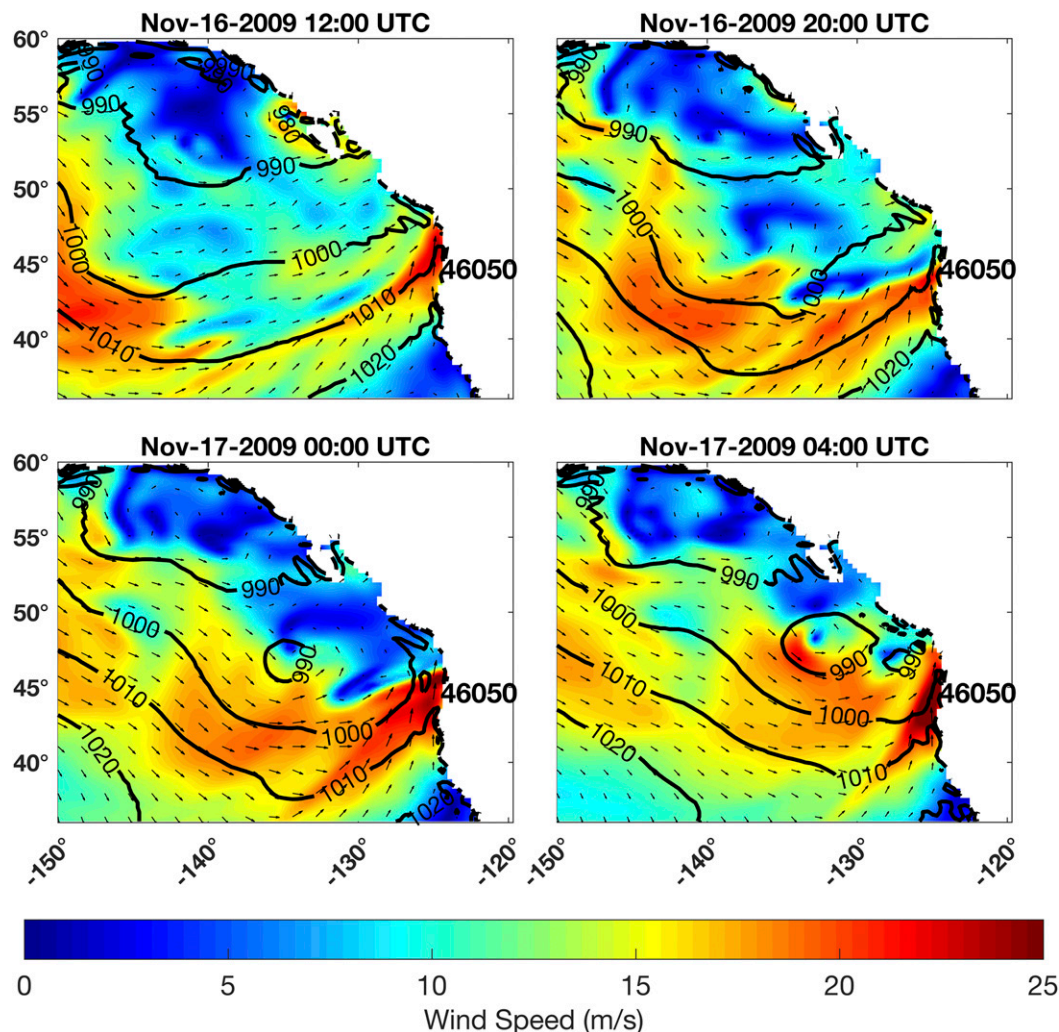


FIG. 3. The synoptic-scale surface pressure and 10-m wind forcing during event 1 from the CFSR. The colors are wind magnitude, and the contours are pressure (mb). NDBC buoy 46050 is also indicated. Note the (top left) low pressure system centered over Graham Island, (top right) the weakening of the southerly wind, (bottom left) the formation of a low pressure system, and (bottom right) the approach of two low pressure systems and strengthening of the southerly wind.

low pressure system at approximately 990 mb forms approximately 700 km west-northwest of NDBC buoy 46050. This low pressure system slowly tracks northeast as the southerly wind increases in speed to over  $25 \text{ ms}^{-1}$  and increases in latitudinal extent. A third, smaller low pressure center at 990 mb forms by 0400 UTC 17 November, 400 km north-northwest of NDBC buoy 46050. At this point, the southerly wind extends along the entire Washington and Oregon coastline and reaches wind speeds greater than  $25 \text{ ms}^{-1}$ . The storm has tracked over land by 0900 UTC 17 November. The low pressure centers coalesce and move toward Vancouver Island, and the southerly wind weakens and ceases to exist by 1000 UTC 17 November.

Local conditions at NDBC buoy 46050 begin with an  $H_s$  of 5 m, an MWD of approximately  $230^\circ$ , and a  $T_m$  of 7.5 s. The wind is southerly, coming from  $180^\circ$  at a speed of  $15 \text{ ms}^{-1}$ . As the  $H_s$  grows, the  $T_m$  increases, and the MWD becomes aligned with the wind. Concurrently, the southerly wind increases in speed, reaching just over  $20 \text{ ms}^{-1}$  at its peak wind speed at 0400 UTC 17 November (as illustrated in the last panel in Fig. 3). After the low pressure systems coalesce and travel over Vancouver Island, the wind drops rapidly and changes direction. It is at this point that the  $H_s$  reaches a maximum of approximately 9 m at 0600 UTC 17 November. At the  $H_s$  maximum, MWD is from approximately  $210^\circ$  (south-southwest), and  $T_m$  is at 9 s. After the event peak,  $H_s$  declines quickly, and the MWD reaches  $240^\circ$  by the end



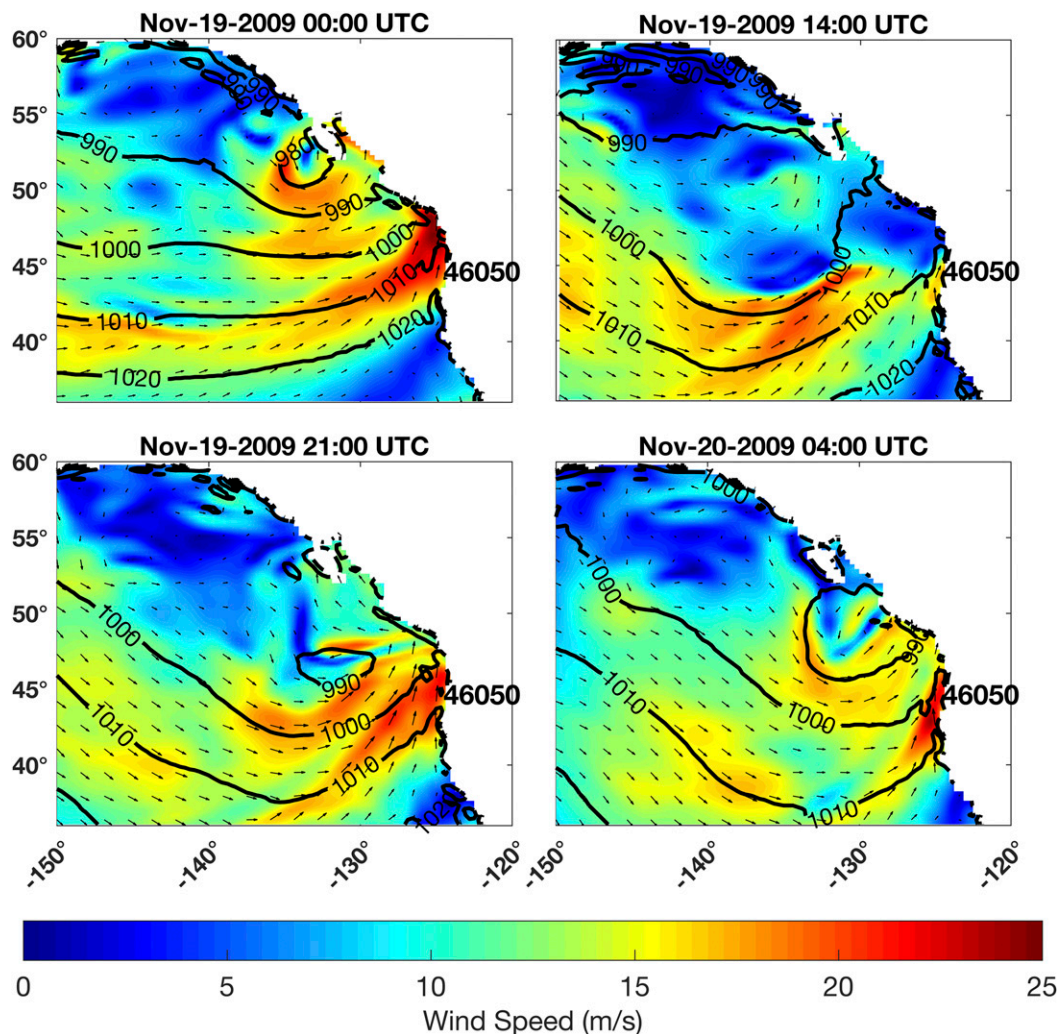


FIG. 4. The synoptic-scale surface pressure and 10-m wind forcing during event 2 from the CFSR. The colors are wind magnitude, and the contours are pressure (mb). NDBC buoy 46050 is also indicated. Note the (top left) low pressure system centered near Graham Island, (top right) the weakening of the southerly wind, (bottom left) the formation of a low pressure system, and (bottom right) this low pressure system's translation to the northeast. The southerly wind in this event does not reach the same wind speeds or latitudinal extent as the southerly wind in the first event.

of the time series. Throughout this time period,  $T_m$  remains at approximately 9 s.

#### b. Event 2

As opposed to event 1, this event is characterized by a weaker southerly wind; the southerly wind dissipates almost entirely and then regenerates with lesser intensity and a smaller latitudinal extent than the southerly wind associated with event 1. The event begins with a low pressure system of 970 mb focused on Graham Island and southerly winds extending from the Oregon–California border to Vancouver Island at 0000 UTC 19 November 2009 (see Fig. 4 for synoptic-scale pressure and wind maps from the CFSR). The

southerly wind dissipates as the low pressure system travels north, and traces of it exist only along the central Oregon coast by 1400 UTC 19 November. The southerly wind then reforms as another low pressure system approaches the coast northwest of NDBC buoy 46050 by 2100 UTC 19 November. At 0500 UTC 20 November, the southerly wind reaches its maximum extent. At this point, it spans the entire Oregon coastline and part of the southern Washington coast, and wind speeds reach between 20 and  $25 \text{ m s}^{-1}$ . As the low pressure system slides over Vancouver Island, the southerly wind decreases appreciably in strength and size by 1000 UTC 20 November.

In contrast to the  $H_s$  associated with events 1 and 3, which increase and decrease rapidly, the  $H_s$  associated with

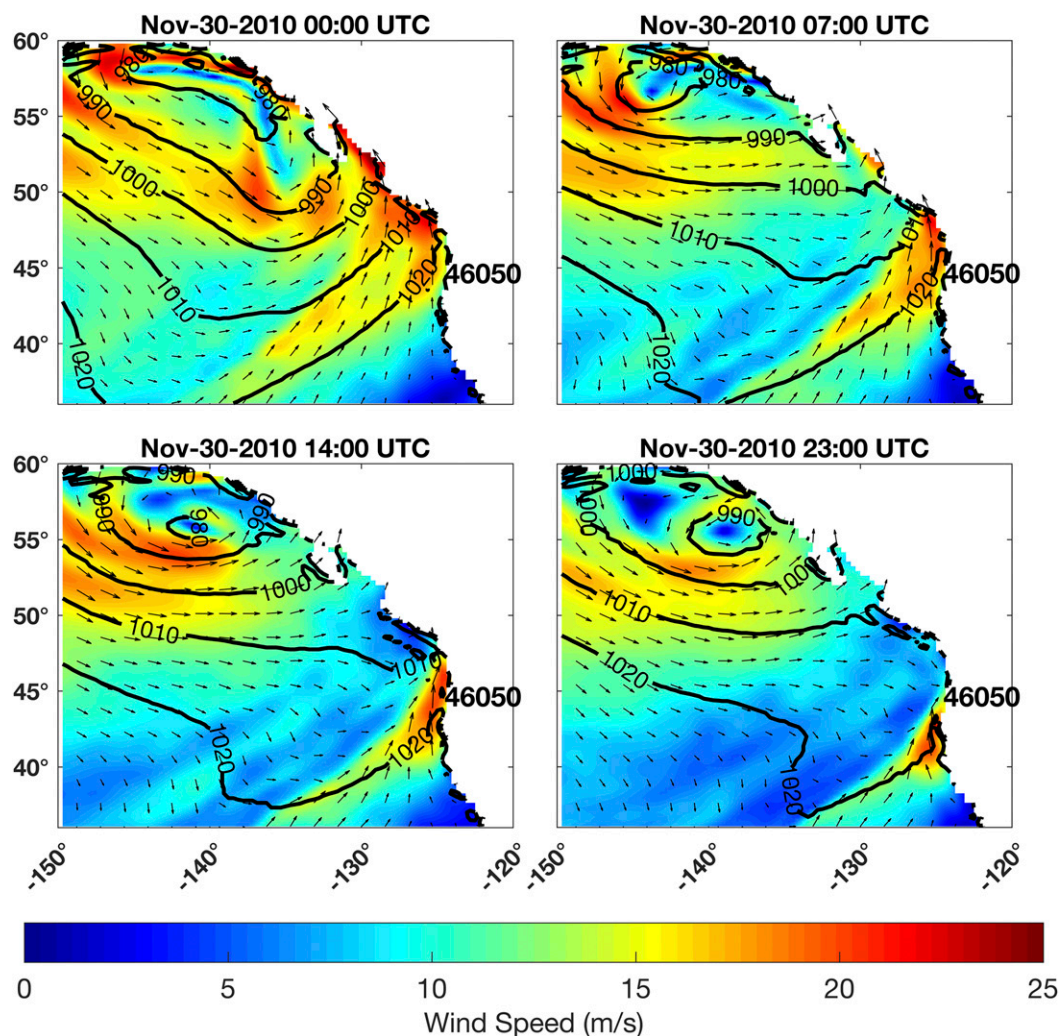


FIG. 5. The synoptic-scale surface pressure and 10-m wind forcing during event 3 from the CFSR. The colors are wind magnitude, and the contours are pressure (mb). NDBC buoy 46050 is also indicated. Note (top left) the low pressure system in the Gulf of Alaska, (top right) the tightening of this system and formation of the southerly wind, (bottom left) further tightening of this system and translation of the southerly wind to the south, and (bottom right) the weakening of both the low pressure system and the southerly wind with respect to pressure level and spatial extent, respectively.

event 2 is sustained at a relatively constant level for approximately 24 h. Bulk parameter wave conditions at NDBC buoy 46050 (see Fig. 2) begin with an  $H_s$  of approximately 4.5 m, an MWD coming from the west-southwest at  $240^\circ$ , and a  $T_m$  of approximately 7.5 s. The wind signal begins as southerly at  $180^\circ$  and at a speed of approximately  $18 \text{ m s}^{-1}$ . As  $H_s$  increases to exceed 6 m within 6 h, the MWD decreases to indicate wave energy incident from a more southern direction, reaching  $220^\circ$ , and the  $T_m$  increases slightly to approximately 8 s. For the remainder of the event, the bulk parameters remain at these values, approximately 6–7 m for  $H_s$ ,  $200^\circ$ – $220^\circ$  (south-southwest) for MWD, and 8 s for  $T_m$ . The wind remains southerly at approximately  $18 \text{ m s}^{-1}$  during the entire event. The

decrease and direction change of the wind coincides with a decrease in  $H_s$  at the end of the event.

### c. Event 3

As opposed to the cyclones of events 1 and 2, which are situated between 400 and 1200 km from NDBC buoy 46050, the cyclone of event 3 is farther away, situated at an additional 1000 km northwest of Graham Island in the Gulf of Alaska. The event begins at 0000 UTC 30 November 2010, with the low pressure system at 980 mb (see Fig. 5 for synoptic-scale pressure and wind maps from the CFSR). As the low pressure center tightens, a southerly wind forms by 0700 UTC, extending from Vancouver Island to the Oregon–California border. The southerly wind reaches speeds of  $20 \text{ m s}^{-1}$ .

The low pressure system travels southeast toward Graham Island as the southerly wind tightens longitudinally, from originally spanning  $3^\circ$  at 0800 UTC 30 November to less than a degree by 2000 UTC 30 November. The southerly wind feature also translates south, extending to NDBC buoy 46050 from the California–Oregon border before dissipating entirely.

The third event is similar to event 1 in that  $H_s$  grows substantially to reach a maximum over the course of several hours. However, unlike events 1 and 2, the  $T_m$  and wind values also grow substantially as opposed to remaining consistent throughout the event. Wave conditions begin with  $H_s$  at 2.5 m,  $T_m$  of 5 s, and MWD at approximately  $210^\circ$ . The wind speed is  $5 \text{ m s}^{-1}$  and is southerly, at  $180^\circ$ , at this point. As  $H_s$  grows to reach 7.5 m in 18 h, the  $T_m$  and wind speed also grow to reach 8 s and almost  $20 \text{ m s}^{-1}$  at the  $H_s$  peak (see Fig. 2). The increase in these parameters coincides with the southward translation of the southerly wind. The MWD remains entirely from the south at  $220^\circ$  throughout the event. After the  $H_s$  peak, both the wind speed and  $H_s$  decrease dramatically, while  $T_m$  increases slightly to 9 s, and the MWD remains from the south.

## 5. Results

In this section, we first document the skill displayed by the various model configurations in predicting the conditions during the identified large wave events. The objective is to identify which combination of input wind field and model physics best reproduces the observed bulk parameters as well as providing an accurate description of the wave spectra. We pay special attention to whether or not the maximum wave height magnitude and timing are reproduced and also analyze how wave energy approaching from different directions is described. We then move on to identifying how improvements in the wind field (by moving from GFS to CFSR) or improvements in the model physics (from ST2 to ST4) affect the results. In other words, we seek to establish how improvements in the results are linked to the quality of the wind input or the adequacy of the wave model physics. The findings will, therefore, not only point toward the most effective model configuration, but also suggest areas of improvement for the wind products as well as potential remaining shortcomings in the model physics that could be remedied with additional research.

The three events, selected for featuring a strong southerly wind and wave heights greater than 6 m, were simulated with the model configurations described in section 3. The bulk parameters ( $H_s$ ,  $T_m$ ) and spectral output of the models will be compared to observations from NDBC buoy 46050 (see Fig. 1), as described in section 3.

### a. Model performance: Bulk parameters

The  $H_s$  time series output of each model configuration for each event is presented in Fig. 6. The differences between the output of the model configurations are in the timing and magnitude of the peak  $H_s$ . For all time series, ST2-GFS yields the lowest peak  $H_s$  values, while configurations ST2-CFSR, ST4-GFS, and ST4-CFSR yield successively greater magnitudes of  $H_s$ . For event 1, the original model estimates the peak  $H_s$  to occur several hours after, and several meters below, the observed peak. When the CFSR wind is utilized with the original physics package (ST2-CFSR), the peak  $H_s$  value increases, but the temporal delay is still present. Elimination of the delay occurs with the implementation of the ST4 physics package and original wind product in ST4-GFS, but the peak  $H_s$  is still underestimated. The combination of the CFSR wind and ST4 physics package in the ST4-CFSR model configuration both eliminates the delay and increases the peak  $H_s$  magnitude, although it still ultimately underestimates the peak by approximately 1 m.

For event 2, the original model output has similar temporal delay and underestimation issues. These issues are ameliorated by the other model configurations, ST2-CFSR and ST4-GFS. However, in contrast with event 1, the  $H_s$  values are overestimated by ST4-CFSR. For event 3, the original model output does not have the timing delay seen in events 1 and 2, but underestimation of  $H_s$  occurs by 2 m. While the peak wave height is better estimated by the other model configurations, the timing of the peak  $H_s$  actually becomes more inaccurate. These model configurations predict the peak to occur before it actually does. Ultimately, the ST4-CFSR model configuration predicts the greatest magnitude peak  $H_s$  but predicts it to occur several hours before the observed peak  $H_s$ .

The error metrics RMSE, percent error (PE), and bias (as defined in García-Medina et al. 2014) for the data from the three events combined show that the ST4 model configurations output results in a lower RMSE for  $H_s$  than the RMSE associated with the output of the ST2 model configurations (see Fig. 9, the columns labeled “All  $H_s$ ” and “All  $T_m$ ”). Also of note is that bias for  $H_s$  switches to become positive for ST4-CFSR. Even though this model configuration predicts the peak wave height value most accurately between the four model configurations for events 1 and 3, it tends to overestimate for moderate wave heights, resulting in an overall positive bias.

### b. Model performance: Energy spectra

The spectra at the time of the maximum wave height are illustrated in Fig. 7. The spectra reproduced in Fig. 7 are



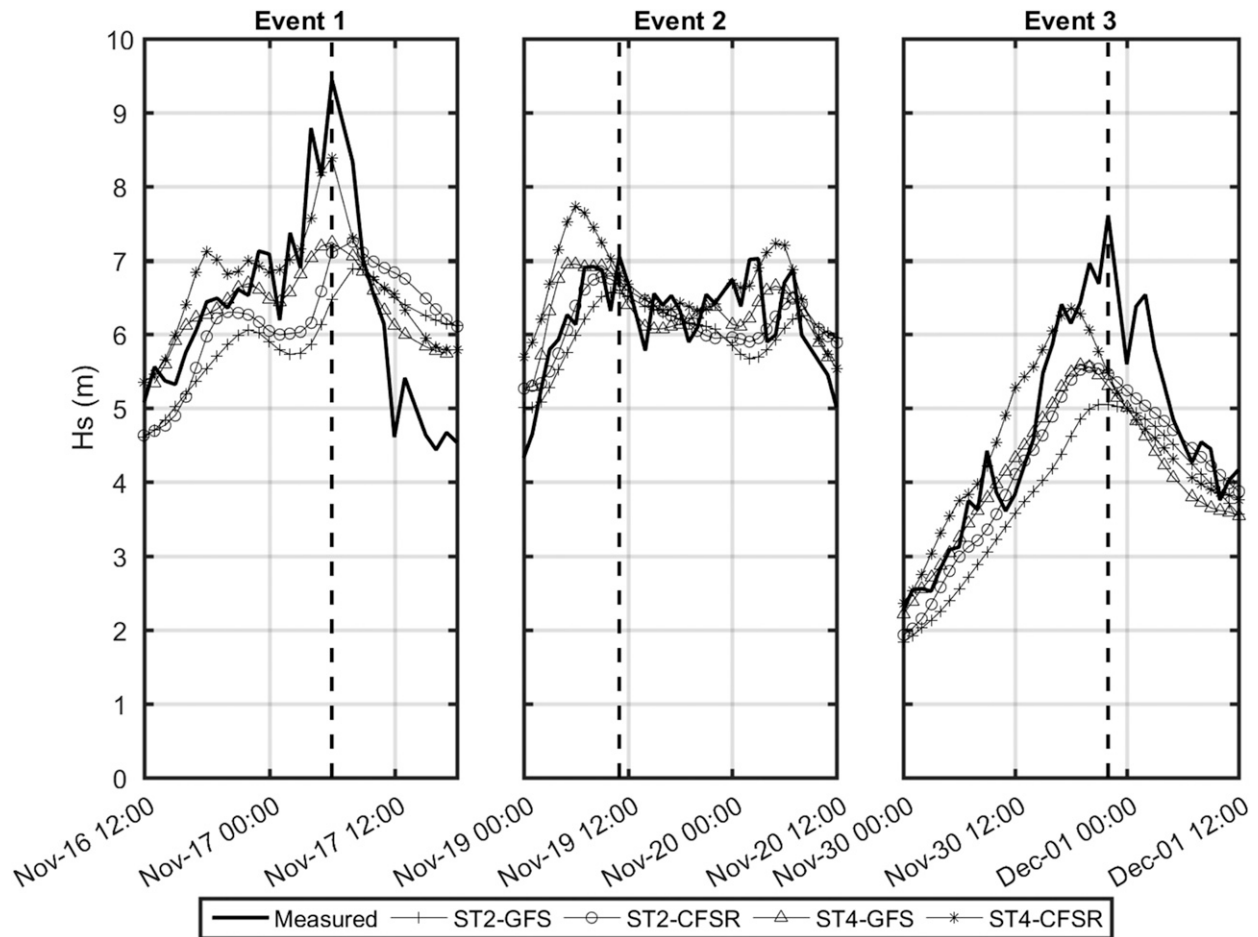


FIG. 6. Time series of  $H_s$  of each model configuration. The vertical dashed line corresponds to the peak of the event and the time of the spectrum illustrated in Fig. 7.

those of the original model configuration (ST2-GFS), the model configuration that performs best for the largest wave heights (ST4-CFSR), and as observed by NDBC buoy 46050. Each spectrum is delineated at  $120^\circ$  and then again at either  $260^\circ$  (for events 1 and 3) or  $240^\circ$  (for event 2), as illustrated in Fig. 8. We selected the second limit,  $260^\circ$  or  $240^\circ$ , after inspecting hourly snapshots of each spectrum and subjectively determining the delineating direction that best bounds the discrete peaks in the spectrum, especially when multiple peaks are present. The first region,  $0^\circ$ – $120^\circ$ , entails energy traveling away from land. The second region,  $120^\circ$ – $240^\circ$  or  $260^\circ$ , represents energy traveling from the south, or “southern” energy, while the third region,  $240^\circ$  or  $260^\circ$ – $360^\circ$ , represents energy traveling from the north, or “northern” energy.

Generally, the spectra associated with the buoy are spread in direction more severely than the spectra associated with the models. This is a repercussion of the directional distribution function implemented in the 2D

wave spectra analysis, which is a directional Fourier series approach as suggested by NDBC. In this method, originally developed by Longuet-Higgins et al. (1963), the directional wave spectrum is represented by a directional Fourier series expansion. The directional distribution  $D(f, \theta)$  (where  $f$  indicates frequency and  $\theta$  indicates direction) is obtained by converting buoy heave, pitch, and roll motions into buoy slope time series using buoy azimuth. From these time series, spectra and cross spectra are calculated, and the first five coefficients of the directional Fourier expansion are derived. The parameters implemented in the directional distribution  $D(f, \theta)$  are then quantified from these coefficients. These directional parameters include  $r_1$ ,  $r_2$ ,  $\theta_1$ , and  $\theta_2$  (Earle et al. 1999). The directional distribution is a cosine spreading function and is given by

$$D(f, \theta) = \frac{1}{\pi} \left\{ \frac{1}{2} + r_1 \cos(\theta - \theta_1) + r_2 \cos[2(\theta - \theta_2)] \right\}. \quad (5)$$



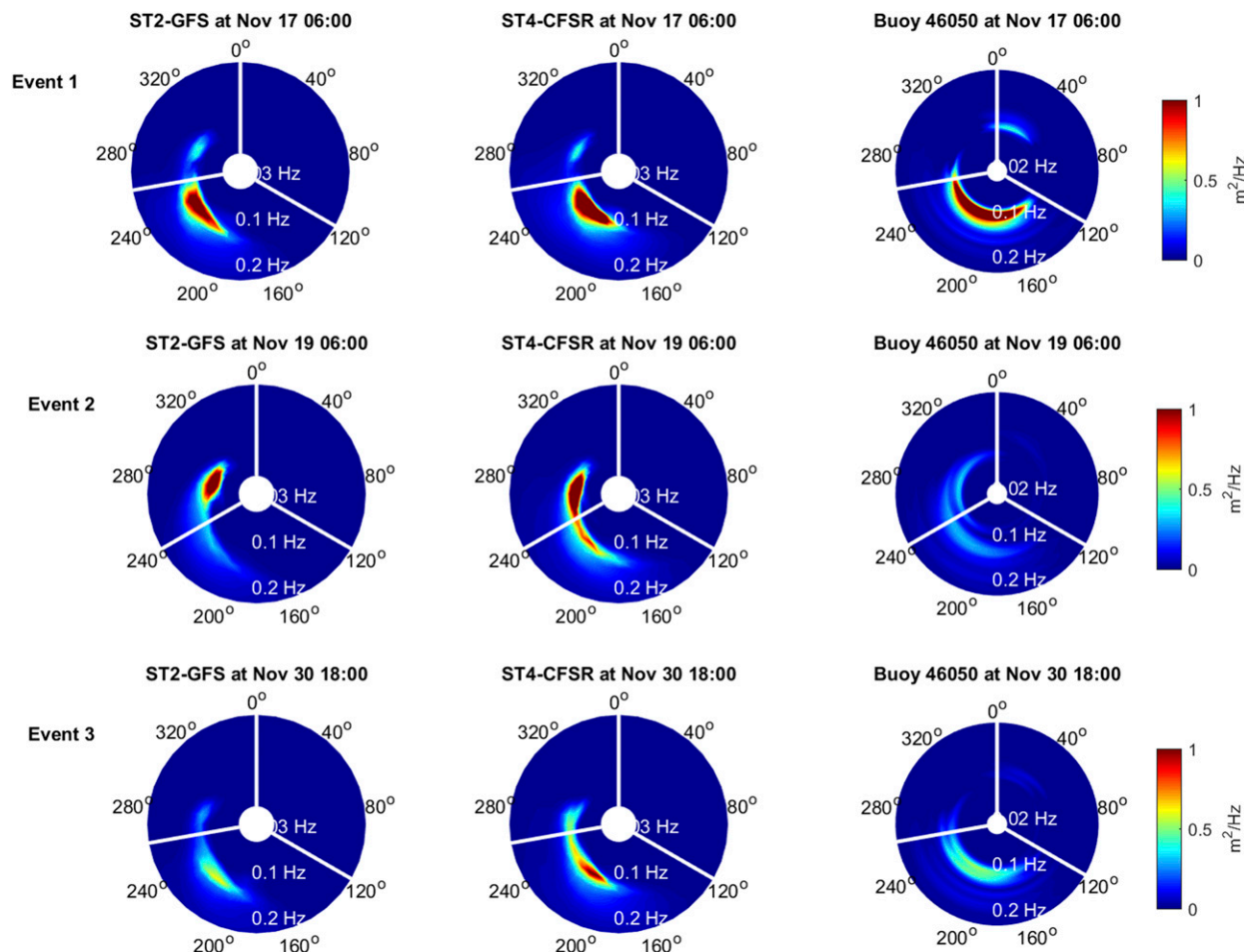


FIG. 7. An example spectra from ST2-GFS, ST4-CFSR, and NDBC buoy 46050 at the peak of each event. The radial axis is the frequency from 0 to 0.2 Hz. Note the observed southern energy at the buoy as compared to this energy as reproduced by ST4-CFSR and ST2-GFS. The directions at which the spectra are delineated are highlighted in white.

The broad directional spread can at times cause the energy associated with the northwest quadrant to “leak” into the southwest quadrant, and no one limit in direction can be determined to avoid this issue altogether. At each time step, an  $H_s$  is computed from the southern and northern quadrants. The time series of the partitioned  $H_s$  and  $T_m$  are then compared and assessed with error statistics. The observed spectra, illustrated in Fig. 7 (right column), show incident wave energy primarily from the south for events 1 and 3, and split between the north and south for event 2. This is consistent with the strong influence of the southerly wind in events 1 and 3. In contrast, the southerly wind is less dominant during event 2 (see Table 2).

The model-generated spectra generally reproduce the primary peak for events 1 and 3, but predict a more energetic northern peak for event 2. For event 1, the model spectra largely agree with the observed spectrum with the greatest concentration of energy in the southern quadrant.

Both model configurations also indicate traces of northern wave energy that do not appear in the observed spectrum. For event 2, the peaks of the observed spectrum occur at different frequencies, with the southern peak at a higher frequency than the northern peak. While the modeled spectral peaks are also associated with slightly different frequencies, the northern peak is of much greater intensity than the southern peak. For event 3, the observed spectrum is unimodal, with the entire peak in the southern quadrant. In contrast, the modeled spectra are bimodal with energy from both the northern and southern quadrants. These peaks are close in direction and of similar frequency. In each case, ST4-CFSR allocates more energy in the southern quadrant, which is associated with energy from the southerly wind, than ST2-GFS.

The spectra analyzed so far represent only one spectral shape for 1 h within the evolution of the event. The energy spectrum can gain intensity in different parts of

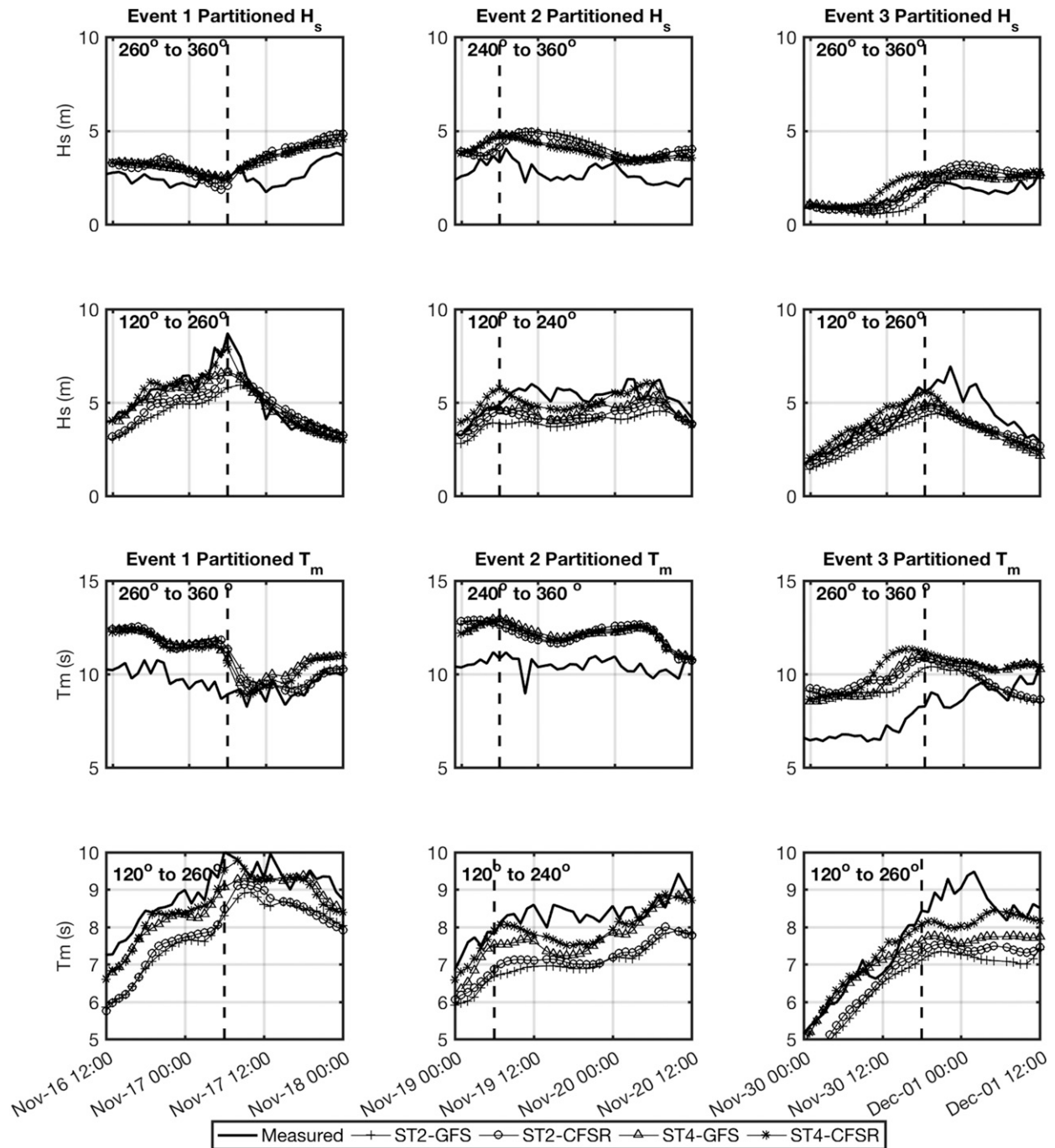


FIG. 8. The  $H_s$  and  $T_m$  time series calculated from spectra partitioned in the southern and northern quadrants. The vertical dashed lines indicate the time of the energy spectra illustrated in Fig. 7. The underestimation of southern energy and overestimation of northern energy is apparent in the  $H_s$  figures. Note the different y axes of the  $T_m$  time series.

the spectrum throughout the event, illustrating the changing character of the wave field. This evolution is summarized by the delineated  $H_s$  and  $T_m$  time series, shown in Fig. 8. The observations of the buoy show that for all three events, the southern  $H_s$  reaches larger values than the northern  $H_s$ . Event 2 differs from events

1 and 3 in that the maximum  $H_s$  values associated with the northern and southern peaks are more similar (4 and 5.5 m for northern and southern  $H_s$ , respectively). The southern  $T_m$  begins at smaller values for events 1 and 2, then increases to reach similar values as the northern  $T_m$ . This is consistent with the notion that southern

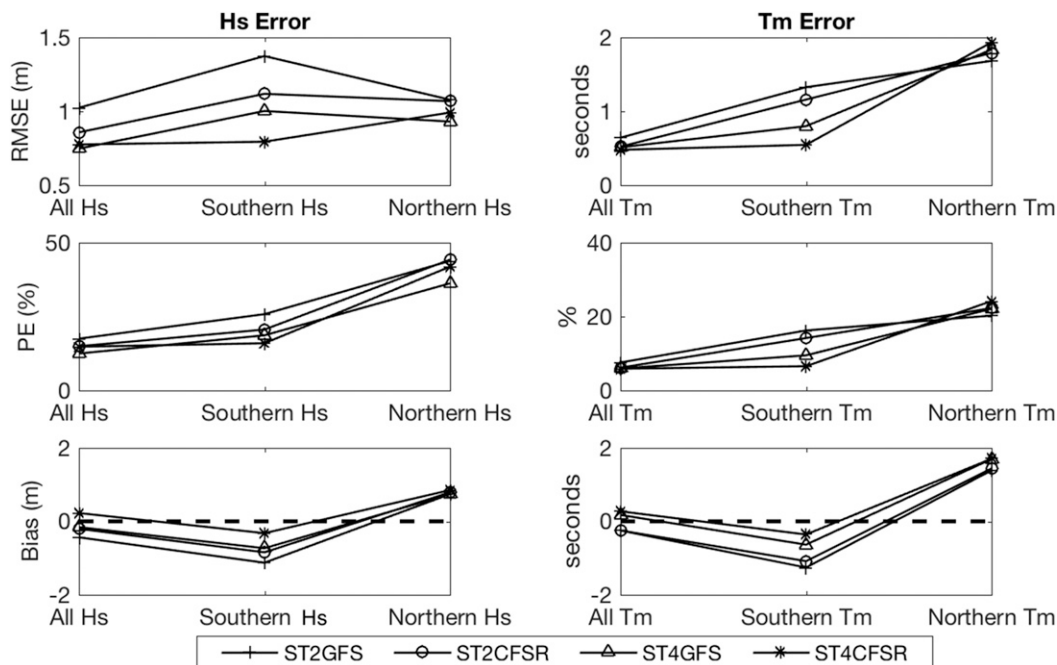


FIG. 9. Error statistics RMSE, PE, and bias with respect to the overall bulk parameters and the partitioned parameters. The data points from the three events are combined for this analysis.

energy is derived from a local wind feature (the southerly wind) that has generated a shorter-period sea state that develops into a midperiod swell. In contrast, the northern wave energy is derived from a distant cyclone that has generated midperiod swell.

The four different model configurations produce similar predictions for the northern  $H_s$  and  $T_m$  that consistently overestimate the observed values by similar amounts for the three events, as represented in the positive bias for the northern bulk parameters (see Fig. 9). In contrast, the southern  $H_s$  values are underestimated in such a way that the individual model configurations produce more differing results. In other words, the variance of the model bias is greater for the southern  $H_s$  than the northern  $H_s$  (see Fig. 9 for partitioned error metrics). This means that the error for the northern  $H_s$  is similar for the various model configurations and so is not sensitive to the specific configuration, while the error for the southern  $H_s$  is smaller for some of the model configurations compared to other configurations and is therefore more sensitive. The original model configuration most severely underestimates the southern  $H_s$  and  $T_m$ . When the original physics package is combined with the CFSR wind, the magnitude of the southern  $H_s$  and  $T_m$  increases. These magnitudes increase more when the original wind and ST4 physics package is implemented in ST4-GFS. The final combination of the ST4 physics package and CFSR wind yields the most accurate southern  $H_s$  and  $T_m$  values. This pattern, where each model configuration

produces a slightly greater magnitude time series, is seen for each event.

While the magnitude of the overestimation of the northern  $H_s$  and  $T_m$  is similar between all model configurations, the times at which peak  $H_s$  values are reached are slightly different. For event 2, the time series associated with the ST4 model configurations reach higher energy values before the time series of the ST2 model configurations. For event 3, akin to the overall bulk parameter time series trends, ST4-CFSR estimates its peak northern and southern  $H_s$  values several hours before the other model configurations estimate their peak  $H_s$  values.

## 6. Discussion

In this section, we explore two additional questions of interest. In particular, we provide more detail about the differences in the wave spectra predictions using the different physics packages. This analysis is especially relevant to individuals who are interested in utilizing the 30-yr hindcast discussed in Chawla et al. (2013a) (assembled using ST2 physics) for the analysis of large wave conditions. Finally, we explore if the improvement in predictions using the CFSR field is linked to the higher spatial or temporal resolution of this product. The answer to this question can inform the development of a new wind forecast product that would be required for more accurate predictions of large waves.

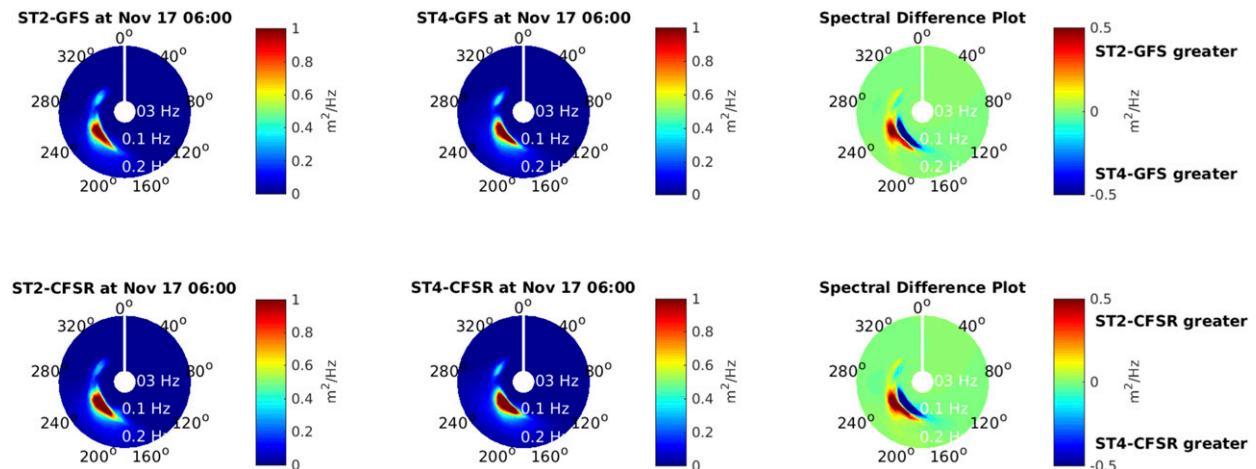


FIG. 10. The spectra as reproduced by the model configurations that implement the same wind package but (left) ST2 and (center) ST4 physics packages. (right) A difference plot of the two spectra.

#### a. Impact of chosen physics package on predictions

The ST4 model configurations outperform the ST2 model configurations with respect to accurately reproducing the southern wave energy, as described in the earlier section. With the ST4 configuration, the southern wave energy associated with the southerly wind as well as the timing of the maximum wave height is captured more accurately. To explore the differences in how the ST2 and ST4 physics packages operate, spectral difference plots between the two are inspected to see where and how the results of the two physics packages differ. The spectra plotted in Fig. 10 are from the peak of event 1. For the same wind product, more energy accumulates in the lower frequencies (and longer periods) for the ST4 spectrum than for the ST2 spectrum. As described above, the southern  $T_m$  is consistently underestimated, and the ST4 configurations better capture the southern  $T_m$  time series by predicting a longer  $T_m$ .

#### b. Impact of chosen wind product on predictions

Inspection of model output with respect to the wind package reveals that the performance is of better quality when the CFSR wind product is implemented (e.g., ST2-GFS vs ST2-CFSR). The CFSR wind package has an increased temporal and spatial resolution as compared with the GFS wind package (see Table 1) and has been reanalyzed with more accurate and detailed physical processes (Saha et al. 2010b). Cross sections of the southerly wind feature associated with each wind package (not shown) indicate that the CFSR produces a steep longitudinal gradient in wind speed that updates hourly to become steeper as the southerly wind tightens. In contrast, the GFS wind cross sections reveal a flatter gradient that remains stagnant even as the southerly wind tightens according to the CFSR wind product. For

example, during event 1, the cross sections of wind taken along latitude at  $44^\circ$  and  $44.64^\circ$  of the CFSR product show wind speeds reaching approximately  $25 \text{ m s}^{-1}$  from  $5 \text{ m s}^{-1}$  in the span of a few degrees. The same cross section shows the GFS wind speeds reaching only  $17 \text{ m s}^{-1}$  from  $10 \text{ m s}^{-1}$  in the same distance. These differences explain why the CFSR wave model configurations produce larger wave heights compared to the GFS wave model.

To explore the relative significance of the spatial or temporal resolution of the wind product on model performance, three variations of ST4-CFSR (hereafter referred to as the “initial” model configuration) are implemented for event 1. These new configurations include variations in the temporal and spatial resolution of the wind product. Similar to the analysis performed in section 5, the respective output is analyzed in terms of bulk parameters and delineated energy spectra.

The first variation, ST4-CFSR-FineGrid, has an increased outermost grid resolution from  $0.5^\circ$  to  $0.312^\circ$ , which matches the resolution of the CFSR wind product. The second variation, ST4-CFSR-CoarseWind, implements a coarser spatial wind input resolution from  $0.312^\circ$  to  $1.9^\circ$  grid resolution. Note that this spatial resolution is even coarser than that of the GFS wind product. The third variation, ST4-CFSR-3hrWind, has a decreased temporal resolution of wind from an hourly input to 3-h input. This case matches the temporal resolution of the GFS wind product and the spatial resolution of the model runs using the GFS winds. The details of these variations are recorded in Table 3.

The output  $H_s$  time series for event 1 for the variations show that severe underestimation occurs with the spatially coarse wind (ST4-CFSR-CoarseWind) (figures not shown). The best performance occurs with the highest resolved grid (ST4-CFSR-FineGrid). Specifically, the



TABLE 3. Variations of ST4-CFSR.

Model name	Outer-grid resolution (°)	Wind	
		Time resolution (h)	Spatial resolution (°)
ST4-CFSR-FineGrid	0.312	1	0.312
ST4-CFSR-3hrWind	0.5	3	0.312
ST4-CFSR-CoarseWind	0.5	1	1.9

results for ST4-CFSR-FineGrid are essentially identical to the initial model configuration (ST4-CFSR) with nearly similar RMSEs. The second variation, ST4-CFSR-3hrWind, performs significantly better than ST4-GFS despite the fact that they both have the same temporal resolution, indicating that the higher quality and finer spatial resolution of the CFSR wind is a greater factor affecting performance than the temporal resolution. This is reinforced by the significantly decreased performance for the larger wave heights for the third variation, ST4-CFSR-CoarseWind (RMSE increases from 0.68 to 2 m). This occurs despite the fact that this simulation implements the higher quality CFSR wind, but on a much coarser grid. The original wind product configuration in ST4-GFS actually outperforms ST4-CFSR-CoarseWind in predicting wave height.

When spectral analysis is performed via delineation (as described in section 5b) and partitioned  $H_s$  and  $T_m$  are calculated, the trends between the northern and southern  $H_s$  time series with respect to the buoy are similar to those trends of the initial ST4-CFSR configuration. The northern  $H_s$  and  $T_m$  are overestimated by all variations by a similar magnitude, suggesting that the model predicts a more developed wave field (with a longer period) than was observed. In contrast, the southern  $H_s$  and  $T_m$  are underestimated. The southern  $H_s$  underestimation is most severe for ST4-CFSR-CoarseWind and least severe for ST4-CFSR-FineGrid. These underestimations reveal that the overall effect of the atmospheric forcing in producing a more developed southern wave field is not completely reproduced.

Overall, the factor that most significantly affects the model performance is the spatial resolution of the wind, as seen by the worse performance of ST4-CFSR-CoarseWind. This signifies that the spatial detail of the atmospheric forcing is important in the model physics. In contrast, the decrease in temporal resolution from 1 to 3 h does not affect the model results significantly as long as the wind field is highly spatially resolved. These findings suggest that a wind product that represents the fine spatial details of the southerly wind is crucial for an accurate prediction of the southern wave energy. Because the southerly wind can be longitudinally narrow, it requires representation in a model that can resolve small longitudinal scales. The GFS product, at a lower resolution than the CFSR product, does not

capture the entirety of the wind feature and its associated peak speed. In contrast, given the residence time of the southerly wind (usually several hours or more), the temporal resolution of either product (1 or 3 h) can adequately resolve the temporal evolution of the southerly wind. A useful further analysis would involve an assessment of the wind products themselves to determine the accuracy with which the separate wind products represent the details of these features. This could, for instance, be accomplished by comparing the wind product winds with satellite observations of the winds. While such an analysis is outside the scope of this study, results presented herein suggest that the accuracy of the wave height predictions is strongly linked to the skill of the wind product in reproducing the details of the relevant features such as the southerly wind.

## 7. Conclusions

Predicting and forecasting large waves can help to mitigate the risks associated with them. The northeast Pacific is an optimal location to study such events, as large wave events occur frequently in this area. This study aimed to understand how state-of-the-art wave models perform when predicting such events by analyzing model performance for three large wave events wherein the significant wave height  $H_s$  exceeds 6 m for longer than 5 h.

The atmospheric conditions that are associated with the analyzed large wave events include a distant cyclone along with a strong southerly wind, which at times appears as a coastal jet. Events 1 and 3 feature this southerly wind at all times, while the southerly wind is more fleeting, is of less intensity, and is of smaller latitudinal extent in event 2. Also, events 1 and 3 are characterized by a strong wave energy signal from the southwest, while event 2 wave energy is divided more equally between waves incident from the northwest and southwest. To explore the importance of various inputs on model performance, different combinations of physics package and wind forcing (Table 1) were utilized in the simulations.

Overall, the ST2-GFS model output is associated with the greatest error, and the ST4-CFSR model configuration best captures the peak wave height in the time series for events 1 and 3. The error metrics for the overall bulk parameters do not show a significant change in

performance between the different model configurations. However, the analysis of wave energy spectra and partitioned bulk parameters clarify the performance of the model configurations for the bulk parameters. The partitioned  $H_s$  and  $T_m$  show that the wave energy from the southwest is stronger, and of a shorter period, than the wave energy from the northwest. The swell arriving from the northwest is more severely overestimated by the model configurations. In contrast, the energetic wind sea, locally driven by the southerly wind, is underestimated by the model configurations. The ST4 model configurations result in more accurate representations of the larger  $H_s$  and longer  $T_m$  values associated with wave energy from the southwest, with the ST4-CFSR model configuration performing best. This could be due to the ST4 physics package allocating more energy into the lower frequencies as compared to the ST2 configurations. These configurations still, however, result in overestimations of the northern wave energy of similar magnitude as the ST2 associated model configurations. The combination of over- and underestimations of the energy from the northern and southern quadrants, respectively, results in a relatively accurate bulk parameter.

We also explored the importance of the resolution of these inputs in model performance by changing their resolution and simulating event 1. We found that increasing the spatial resolution of the grid did not render better model performance, but a decrease of the spatial resolution of the wind input (from  $0.5^\circ$  to  $1.9^\circ$ ) severely decreased model performance. In fact, the spatially coarser wind input affects model performance more severely than does a temporally coarser wind input. This signifies that accurately modeling the wave energy generated by the southerly wind is sensitive to resolving the fine physical details of the southerly wind as opposed to the temporal variability over time scales shorter than 3 h.

In light of these findings, we would recommend the ST4-CFSR model configuration specifically for reproducing the effects of a southerly wind on the wave field. Generally, best practices would incorporate the understanding of the important spatial or temporal scales of a local atmospheric feature and find the optimal combination of a wind product and physics package that best represents the physical processes for each context.

**Acknowledgments.** We would like to acknowledge Jim Thomson and Adam Brown from the Applied Physics Laboratory at the University of Washington, and Merrick Haller from the School of Civil and Construction Engineering at Oregon State University, who offered critical feedback throughout this study. We are also grateful to Gabriel García-Medina for performing the work upon which this study is built. This paper is

based upon work supported by the U.S. Department of Energy under Award DE-EE0006816. Neither the U.S. government nor any agency thereof, nor any of their employees, makes any warranty, expressed or implied, or assumes any legal liability or responsibility for the accuracy, completeness, or usefulness of any information, apparatus, product, or process disclosed, or represents that its use would not infringe upon privately owned rights. Reference herein to any specific commercial product, process, or service by trade name, trademark, manufacturer, or otherwise does not necessarily constitute or imply its endorsement, recommendation, or favoring by the U.S. government or any agency thereof. The views and opinions of the authors expressed herein do not necessarily state or reflect those of the U.S. government or any agency thereof.

## APPENDIX

### Hindcasted Dataset

#### a. Error statistics: All data

This analysis summarizes the performance of a hindcasted dataset discussed in [García-Medina et al. \(2014\)](#). The hindcast spans the years 2005–11. Bulk parameters of significant wave height and energy period are compared to measured bulk parameters. A depiction of an overall scatterplot for the full dataset ( $N = 24695$  data points) is presented in [Fig. A1](#). Statistical values quantifying the comparison include RMSE, PE, bias, and SI. The overall correlation coefficient for  $H_s$  is 0.91, RMSE is 0.50 m, PE is 20%, SI is 0.20, and bias is positive at 0.11 m.

#### b. Error statistics: Binned by wave height

To gain an intuition of statistical trends for wave heights of interest, the dataset is divided into regions of wave heights greater than 6 m, between 4 and 6 m, and less than 4 m. Wave height error statistics are summarized in [Table A1](#).

The RMSE and bias increase as the wave heights increase. Note that this error calculated with respect to binned wave height could reflect either error estimations of wave height or a phase shift in the wave height time series (see [Jiang et al. 2016](#)). The RMSE and bias are significantly greater for data associated with the larger significant wave height, although PE and SI do not demonstrate a significant increase between the smallest and largest wave heights. The model tends to slightly overestimate wave heights less than 4 m (positive bias of 0.14 m), but underestimates wave heights larger than 6 m (negative bias of 0.67 m).

While dividing the data into regions of wave height is helpful to gain a broad understanding of data trends,

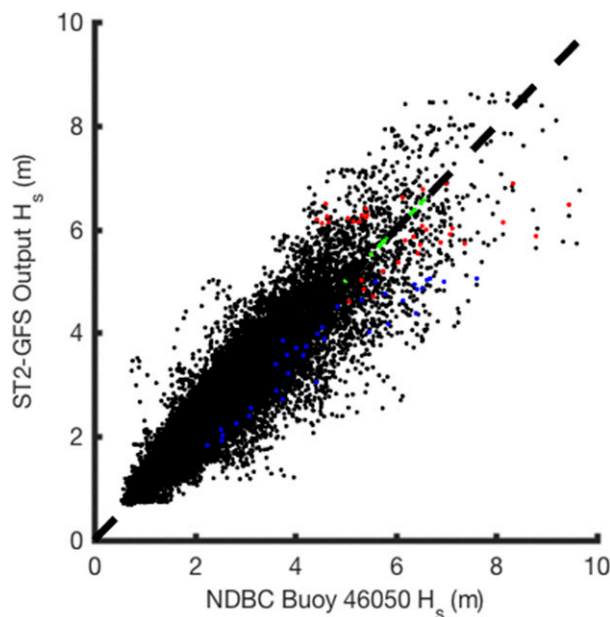


FIG. A1. Scatterplot showing all data points for all years of model hindcast (2005–11). The colored points are the cases considered in this study, where events 1, 2, and 3 are colored red, green, and blue, respectively.

binning the data into tighter divisions may lend more insight into nuances of the error between different wave heights. This is illustrated in Fig. A2, where results are

TABLE A1. Error statistics binned by wave height.

Wave height (m)	<i>N</i>	RMSE (m)	PE (%)	Bias (m)	SI
<4	21 944	0.42	20	0.14	0.2
4–6	2412	0.81	17	−0.03	0.17
≥6	339	1.34	19	−0.67	0.2
Overall	24 695	0.5	20	0.11	0.2

also presented by season to illustrate the differences throughout the year and the associated model performance. Note that there are no data points associated with a wave height of 8.5 m for winter.

The RMSE clearly increases with increasing wave height. These elevated levels of RMSE for wave heights greater than 6 m are due primarily to model error for the largest wave heights. Percent error and SI begin at elevated levels before dropping at 1.5-m significant wave height to reach minimal values between 3 and 5 m for fall, winter, and spring. The elevated levels of PE and SI statistics can be understood as these statistics are normalized by wave height, and the small wave height value thus renders a greater error statistic value for similar absolute errors.

To hone in specifically on the model performance for the greater wave heights and associated energy period dependence, the dataset is divided into “smaller” and “larger” wave height categories (less than 6 m and

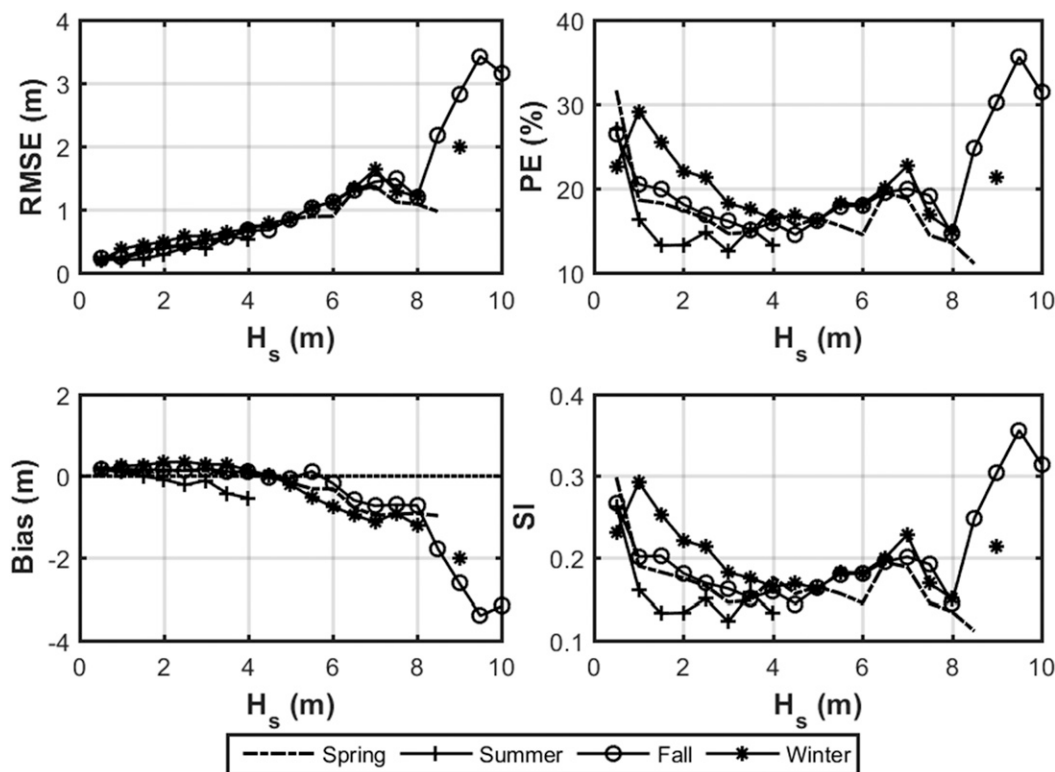


FIG. A2. Error statistics binned by wave height and divided by season.

greater than 6 m), and the results are then binned by energy period. The error statistics are then calculated (figure not shown).

Error statistics exhibit a different trend for the larger and smaller wave heights. Overall, greater values are reached for  $H_s \geq 6$  m than  $H_s < 6$  m. The error statistics for the smaller wave heights remain relatively consistent throughout the energy periods until an energy period of about 11 s. At this point, error statistic values diverge depending on the season.

For the larger wave heights, however, data points have the highest error statistic values for either end of the energy period range. The shortest and longest energy periods exhibit the greatest values of SI, PE, and RMSE, as well as the most negative bias. The smallest error statistic values occur for energy periods between 11 and 14 s, signifying that midperiod swell is the region of best model performance. In this region, the bias is slightly positive as opposed to negative at either limit of the energy period values.

## REFERENCES

- Allan, J., and P. Komar, 2000: Are ocean wave heights increasing in the eastern North Pacific? *Eos, Trans. Amer. Geophys. Union*, **81**, 561–567, <https://doi.org/10.1029/EO081i047p00561-01>.
- Alves, J.-H. G., A. Chawla, H. L. Tolman, D. Schwab, G. Lang, and G. Mann, 2014: The operational implementation of a Great Lakes wave forecasting system at NOAA/NCEP. *Wea. Forecasting*, **29**, 1473–1497, <https://doi.org/10.1175/WAF-D-12-00049.1>.
- Amante, C., and B. W. Eakins, 2009: ETOPO1 1 Arc-Minute Global Relief Model: Procedures, data sources and analysis. NOAA Tech. Memo. NESDIS NGDC-24, NOAA/National Geophysical Data Center, <https://doi.org/10.7289/V5C8276M>.
- Ardhuin, F., T. Herbers, K. P. Watts, G. P. Van Vledder, R. Jensen, and H. C. Graber, 2007: Swell and slanting-fetch effects on wind wave growth. *J. Phys. Oceanogr.*, **37**, 908–931, <https://doi.org/10.1175/JPO3039.1>.
- , and Coauthors, 2010: Semiempirical dissipation source functions for ocean waves. Part I: Definition, calibration, and validation. *J. Phys. Oceanogr.*, **40**, 1917–1941, <https://doi.org/10.1175/2010JPO4324.1>.
- Arinaga, R. A., and K. F. Cheung, 2012: Atlas of global wave energy from 10 years of reanalysis and hindcast data. *Renewable Energy*, **39**, 49–64, <https://doi.org/10.1016/j.renene.2011.06.039>.
- Behrens, A., and H. Günther, 2009: Operational wave prediction of extreme storms in northern Europe. *Nat. Hazards*, **49**, 387–399, <https://doi.org/10.1007/s11069-008-9298-3>.
- Bidlot, J.-R., D. J. Holmes, P. A. Wittmann, R. Lalbeharry, and H. S. Chen, 2002: Intercomparison of the performance of operational ocean wave forecasting systems with buoy data. *Wea. Forecasting*, **17**, 287–310, [https://doi.org/10.1175/1520-0434\(2002\)017<0287:IOTPOO>2.0.CO;2](https://doi.org/10.1175/1520-0434(2002)017<0287:IOTPOO>2.0.CO;2).
- , P. Janssen, S. Abdalla, and H. Hersbach, 2007: A revised formulation of ocean wave dissipation and its model impact. ECMWF Tech. Memo. 509, 27 pp., <https://www.ecmwf.int/sites/default/files/elibrary/2007/8228-revised-formulation-ocean-wave-dissipation-and-its-model-impact.pdf>.
- Carignan, K. S., L. A. Taylor, B. W. Eakins, and R. R. Warnken, 2009a: Digital elevation model of Astoria, Oregon: Procedures, data sources and analysis. NOAA Tech. Memo. NESDIS NGDC-25, NOAA/National Geophysical Data Center, Boulder, CO.
- , —, —, —, E. Lim, and P. Grothe, 2009b: Digital elevation model of central Oregon coast: Procedures, data sources and analysis. NOAA Tech. Memo. NESDIS NGDC-25, NOAA/National Geophysical Data Center, Boulder, CO.
- , —, —, —, T. Sazonova, and D. C. Schoolcraft, 2009c: Digital elevation model of Garibaldi, Oregon: Procedures, data sources and analysis. NOAA Tech. Memo. NESDIS NGDC-16, NOAA/National Geophysical Data Center, Boulder, CO.
- , —, —, —, —, and —, 2009d: Digital elevation model of Port Orford, Oregon: Procedures, data sources and analysis. NOAA Tech. Memo. NESDIS NGDC-21, NOAA/National Geophysical Data Center, Boulder, CO.
- Cavaleri, L., 2009: Wave modeling—Missing the peaks. *J. Phys. Oceanogr.*, **39**, 2757–2778, <https://doi.org/10.1175/2009JPO4067.1>.
- Chalikov, D., and M. Y. Belevich, 1993: One-dimensional theory of the wave boundary layer. *Bound.-Layer Meteor.*, **63**, 65–96, <https://doi.org/10.1007/BF00705377>.
- Chawla, A., D. M. Spindler, and H. L. Tolman, 2013a: Validation of a thirty year wave hindcast using the Climate Forecast System Reanalysis winds. *Ocean Modell.*, **70**, 189–206, <https://doi.org/10.1016/j.ocemod.2012.07.005>.
- , and Coauthors, 2013b: A multigrid wave forecasting model: A new paradigm in operational wave forecasting. *Wea. Forecasting*, **28**, 1057–1078, <https://doi.org/10.1175/WAF-D-12-00007.1>.
- Doyle, J. D., 1997: The influence of mesoscale orography on a coastal jet and rainband. *Mon. Wea. Rev.*, **125**, 1465–1488, [https://doi.org/10.1175/1520-0493\(1997\)125<1465:TOMOO>2.0.CO;2](https://doi.org/10.1175/1520-0493(1997)125<1465:TOMOO>2.0.CO;2).
- Earle, M., K. Steele, and D. Wang, 1999: Use of advanced directional wave spectra analysis methods. *Ocean Eng.*, **26**, 1421–1434, [https://doi.org/10.1016/S0029-8018\(99\)00010-4](https://doi.org/10.1016/S0029-8018(99)00010-4).
- Esquivel-Trava, B., F. J. Ocampo-Torres, and P. Osuna, 2015: Spatial structure of directional wave spectra in hurricanes. *Ocean Dyn.*, **65**, 65–76, <https://doi.org/10.1007/s10236-014-0791-9>.
- Fan, Y., S.-J. Lin, I. M. Held, Z. Yu, and H. L. Tolman, 2012: Global ocean surface wave simulation using a coupled atmosphere–wave model. *J. Climate*, **25**, 6233–6252, <https://doi.org/10.1175/JCLI-D-11-00621.1>.
- García-Medina, G., H. T. Özkan-Haller, and P. Ruggiero, 2014: Wave resource assessment in Oregon and southwest Washington, USA. *Renewable Energy*, **64**, 203–214, <https://doi.org/10.1016/j.renene.2013.11.014>.
- Graham, N. E., and H. F. Diaz, 2001: Evidence for intensification of North Pacific winter cyclones since 1948. *Bull. Amer. Meteor. Soc.*, **82**, 1869–1893, [https://doi.org/10.1175/1520-0477\(2001\)082<1869:EFIONP>2.3.CO;2](https://doi.org/10.1175/1520-0477(2001)082<1869:EFIONP>2.3.CO;2).
- Grothe, P. R., and Coauthors, 2010: Digital elevation model of Taholah, Washington: Procedures, data sources, and analysis. NOAA Tech. Memo. NESDIS NGDC-34, NOAA/National Geophysical Data Center, Boulder, CO.
- , L. A. Taylor, B. W. Eakins, K. S. Carignan, R. J. Caldwell, E. Lim, and D. Z. Friday, 2011: Digital elevation models of Crescent City, California: Procedures, data sources, and analysis. NOAA Tech. Memo. NESDIS NGDC-51, NOAA/National Geophysical Data Center, Boulder, CO.



- Gyakum, J. R., J. R. Anderson, R. H. Grumm, and E. L. Gruner, 1989: North Pacific cold-season surface cyclone activity: 1975–1983. *Mon. Wea. Rev.*, **117**, 1141–1155, [https://doi.org/10.1175/1520-0493\(1989\)117<1141:NPCSSC>2.0.CO;2](https://doi.org/10.1175/1520-0493(1989)117<1141:NPCSSC>2.0.CO;2).
- Hasselmann, S., and K. Hasselmann, 1985: Computations and parameterizations of the nonlinear energy transfer in a gravity-wave spectrum. Part I: A new method for efficient computations of the exact nonlinear transfer integral. *J. Phys. Oceanogr.*, **15**, 1369–1377, [https://doi.org/10.1175/1520-0485\(1985\)015<1369:CAPOTN>2.0.CO;2](https://doi.org/10.1175/1520-0485(1985)015<1369:CAPOTN>2.0.CO;2).
- Hu, K., and Q. Chen, 2011: Directional spectra of hurricane-generated waves in the Gulf of Mexico. *Geophys. Res. Lett.*, **38**, L19608, <https://doi.org/10.1029/2011GL049145>.
- Innocentini, V., E. Caetano, and J. T. Carvalho, 2014: A procedure for operational use of wave hindcasts to identify landfall of heavy swell. *Wea. Forecasting*, **29**, 349–365, <https://doi.org/10.1175/WAF-D-13-00077.1>.
- Janssen, P. A., 1991: Quasi-linear theory of wind-wave generation applied to wave forecasting. *J. Phys. Oceanogr.*, **21**, 1631–1642, [https://doi.org/10.1175/1520-0485\(1991\)021<1631:QLTOWW>2.0.CO;2](https://doi.org/10.1175/1520-0485(1991)021<1631:QLTOWW>2.0.CO;2).
- Jiang, H., A. V. Babanin, and G. Chen, 2016: Event-based validation of swell arrival time. *J. Phys. Oceanogr.*, **46**, 3563–3569, <https://doi.org/10.1175/JPO-D-16-0208.1>.
- Kazeminezhad, M. H., and S. M. Siadatmousavi, 2017: Performance evaluation of WAVEWATCH III model in the Persian Gulf using different wind resources. *Ocean Dyn.*, **67**, 839–855, <https://doi.org/10.1007/s10236-017-1063-2>.
- Komar, P. D., and J. Allan, 2000: Analyses of extreme waves and water levels on the Pacific Northwest coast. Rep. to the Oregon Department of Land Conservation and Development, 24 pp., <https://digital.osl.state.or.us/islandora/object/osl:3952>.
- Kpogo-Nuwoklo, K. A., M. Olagnon, and Z. Guédé, 2014: Wave spectra partitioning and identification of wind sea and swell events. *33rd Int. Conf. on Ocean, Offshore and Arctic Engineering*, San Francisco, CA, American Society of Mechanical Engineers, V04BT02A058.
- Kuik, A., G. P. Van Vledder, and L. Holthuijsen, 1988: A method for the routine analysis of pitch-and-roll buoy wave data. *J. Phys. Oceanogr.*, **18**, 1020–1034, [https://doi.org/10.1175/1520-0485\(1988\)018<1020:AMFTRA>2.0.CO;2](https://doi.org/10.1175/1520-0485(1988)018<1020:AMFTRA>2.0.CO;2).
- Kumar, V. S., G. Johnson, G. U. Dora, S. P. Chempalayil, J. Singh, and P. Pednekar, 2012: Variations in nearshore waves along Karnataka, west coast of India. *J. Earth Syst. Sci.*, **121**, 393–403, <https://doi.org/10.1007/s12040-012-0160-3>.
- Longuet-Higgins, M. S., D. E. Cartwright, and N. D. Smith, 1963: Observations of the directional spectrum of sea waves using the motions of a floating buoy. *Ocean Wave Spectra*, Prentice-Hall, 111–136.
- Menéndez, M., F. J. Méndez, I. J. Losada, and N. E. Graham, 2008: Variability of extreme wave heights in the northeast Pacific Ocean based on buoy measurements. *Geophys. Res. Lett.*, **35**, L22607, <https://doi.org/10.1029/2008GL035394>.
- Monbaliu, J., R. Padilla-Hernandez, J. C. Hargreaves, J. C. C. Albiach, W. Luo, M. Sclavo, and H. Guenther, 2000: The spectral wave model, WAM, adapted for applications with high spatial resolution. *Coastal Eng.*, **41**, 41–62, [https://doi.org/10.1016/S0378-3839\(00\)00026-0](https://doi.org/10.1016/S0378-3839(00)00026-0).
- Moon, I.-J., I. Ginis, T. Hara, H. L. Tolman, C. Wright, and E. J. Walsh, 2003: Numerical simulation of sea surface directional wave spectra under hurricane wind forcing. *J. Phys. Oceanogr.*, **33**, 1680–1706, <https://doi.org/10.1175/2410.1>.
- NCEP/NWS, 2007: NCEP Global Forecast System (GFS) analyses and forecasts. Research Data Archive, Computational and Information Systems Laboratory, National Center for Atmospheric Research, Boulder, CO, accessed 15 December 2015, <https://doi.org/10.5065/D65Q4TSG>.
- Padilla-Hernández, R., W. Perrie, B. Toulany, and P. Smith, 2007: Modeling of two northwest Atlantic storms with third-generation wave models. *Wea. Forecasting*, **22**, 1229–1242, <https://doi.org/10.1175/2007WAF2005104.1>.
- Portilla, J., 2012: Storm-source-locating algorithm based on the dispersive nature of ocean swells. *Avances*, **4**, C22–C36.
- Rapizo, H., A. V. Babanin, E. Schulz, M. A. Hemer, and T. H. Durrant, 2015: Observation of wind-waves from a moored buoy in the Southern Ocean. *Ocean Dyn.*, **65**, 1275–1288, <https://doi.org/10.1007/s10236-015-0873-3>.
- Rascle, N., F. Ardhuin, P. Queffelec, and D. Croizé-Fillon, 2008: A global wave parameter database for geophysical applications. Part 1: Wave-current–turbulence interaction parameters for the open ocean based on traditional parameterizations. *Ocean Modell.*, **25**, 154–171, <https://doi.org/10.1016/j.ocemod.2008.07.006>.
- Rogers, W. E., J. M. Kaihatu, L. Hsu, R. E. Jensen, J. D. Dykes, and K. T. Holland, 2007: Forecasting and hindcasting waves with the SWAN model in the Southern California Bight. *Coastal Eng.*, **54**, 1–15, <https://doi.org/10.1016/j.coastaleng.2006.06.011>.
- Ruggiero, P., P. D. Komar, and J. C. Allan, 2010: Increasing wave heights and extreme value projections: The wave climate of the U.S. Pacific Northwest. *Coastal Eng.*, **57**, 539–552, <https://doi.org/10.1016/j.coastaleng.2009.12.005>.
- Saha, S., and Coauthors, 2010a: NCEP Climate Forecast System Reanalysis (CFSR) selected hourly time-series products, January 1979 to December 2010. Research Data Archive, Computational and Information Systems Laboratory, National Center for Atmospheric Research, Boulder, CO, accessed 15 December 2015, <https://doi.org/10.5065/D6513W89>.
- , and Coauthors, 2010b: The NCEP Climate Forecast System Reanalysis. *Bull. Amer. Meteor. Soc.*, **91**, 1015–1058, <https://doi.org/10.1175/2010BAMS3001.1>.
- Seymour, R. J., 2011: Evidence for changes to the northeast Pacific wave climate. *J. Coastal Res.*, **27**, 194–201, <https://doi.org/10.2112/JCOASTRES-D-09-00149.1>.
- Stopa, J. E., and K. F. Cheung, 2014: Intercomparison of wind and wave data from the ECMWF Reanalysis Interim and the NCEP Climate Forecast System Reanalysis. *Ocean Modell.*, **75**, 65–83, <https://doi.org/10.1016/j.ocemod.2013.12.006>.
- Timmermans, B., D. Stone, M. Wehner, and H. Krishnan, 2017: Impact of tropical cyclones on modeled extreme wind-wave climate. *Geophys. Res. Lett.*, **44**, 1393–1401, <https://doi.org/10.1002/2016GL071681>.
- Tolman, H. L., 2009: User manual and system documentation of WAVEWATCH III version 3.14. NCEP Tech. Note, MMAB Contribution 276, 220 pp., [http://polar.ncep.noaa.gov/mmab/papers/tn276/MMAB\\_276.pdf](http://polar.ncep.noaa.gov/mmab/papers/tn276/MMAB_276.pdf).
- , and D. Chalikov, 1996: Source terms in a third-generation wind wave model. *J. Phys. Oceanogr.*, **26**, 2497–2518, [https://doi.org/10.1175/1520-0485\(1996\)026<2497:STIATG>2.0.CO;2](https://doi.org/10.1175/1520-0485(1996)026<2497:STIATG>2.0.CO;2).
- , J.-H. G. Alves, and Y. Y. Chao, 2005: Operational forecasting of wind-generated waves by Hurricane Isabel at NCEP. *Wea. Forecasting*, **20**, 544–557, <https://doi.org/10.1175/WAF852.1>.
- Wolf, J., 2009: Coastal flooding: Impacts of coupled wave–surge–tide models. *Nat. Hazards*, **49**, 241–260, <https://doi.org/10.1007/s11069-008-9316-5>.